Hybrid Force-Position Control of the Motion Compensated Gangway

B. Walgaard

Master of Science Thesis

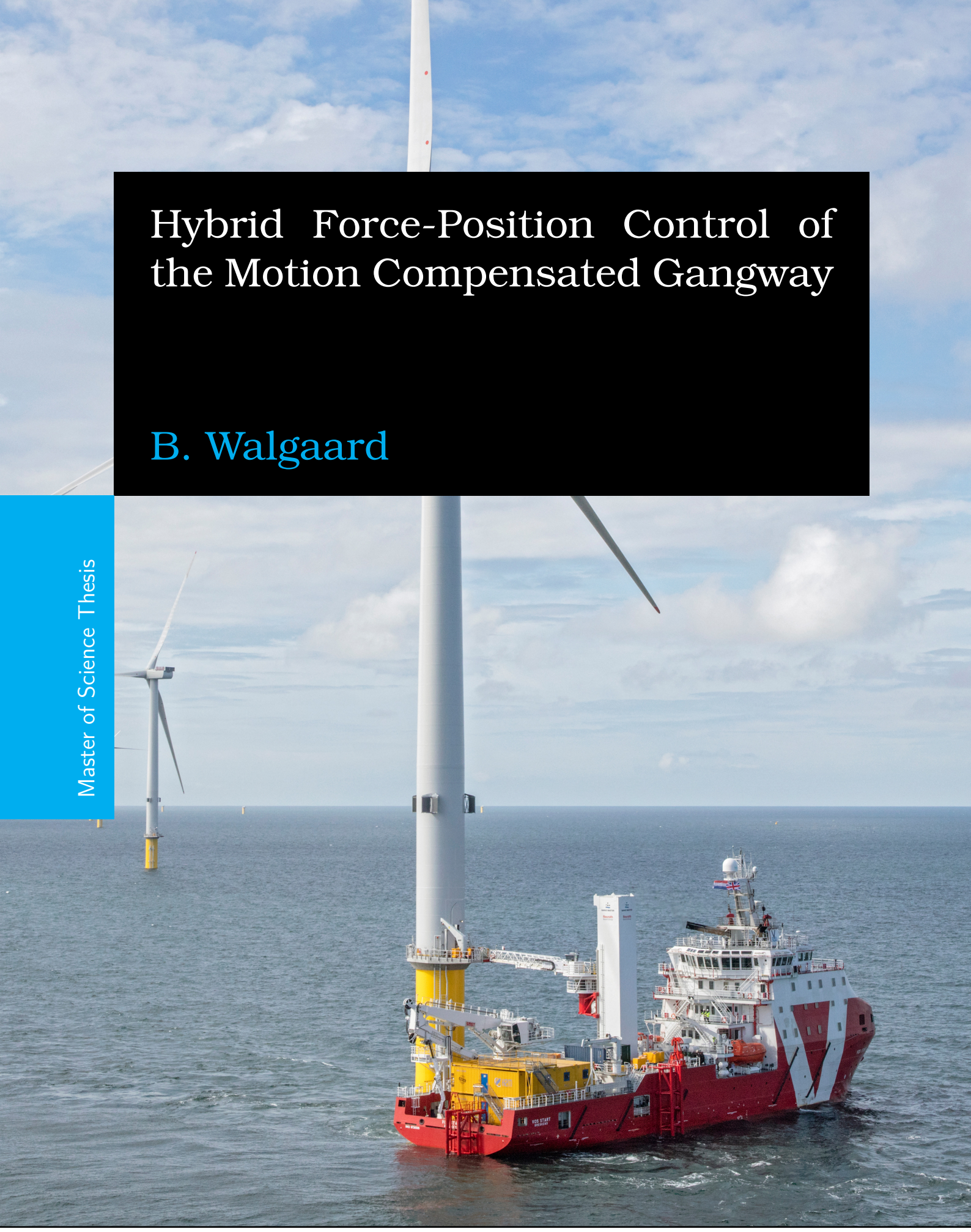

TU Delft Delft University of Technology

Delft Center for Systems and Control

Hybrid Force-Position Control of the Motion Compensated Gangway

Master of Science Thesis

For the degree of Master of Science in Systems and Control at Delft University of Technology

B. Walgaard

November 21, 2017

Faculty of Mechanical, Maritime and Materials Engineering (3mE) · Delft University of Technology

BARGE MASTER

The work in this thesis was supported by Barge Master B.V. Their cooperation is hereby gratefully acknowledged.

Copyright © Delft Center for Systems and Control (DCSC)
All rights reserved.

Abstract

Motion compensation for personnel transfer has greatly reduced costs and increased accessibility for offshore assets operation and maintenance. Solutions exist using hexapods or gangways that make a stiff connection by clamping to a customized offshore structure. State of the art gangways allow for a stepless workflow and have a rubber tip which does not require specialized landing structures. However, in these solutions contact force variations are high. This results in a reduction of safety due to the loss of contact or slipping motions. Therefore, a system with force sensors in the tip is proposed. This allows for the tip forces to be used in feedback control. Literature on this subject describes hydraulic actuator force control, impedance control, or force control in free moving robotics. Literature fails to describe suitable solutions to the hydraulic force control problem where motions are dictated and force tracking is required. In this thesis the dynamic problem of force-position control with hydraulics is simplified, allowing linear analysis and controller design. A 3D model has been created and used to show the need for force feedback after which an analysis is performed on the actuator dynamics. The root locus method is used to close the force control loop with a proportional-integral controller. This results in a complete force-position control structure which tracks a force setpoint on a moving object. The controller structure has been implemented during sea trials and showed significant improvement in the force control performance. This approach of force control using hydraulic actuation is expected to significantly increase safety in offshore operations.

Table of Contents

List of Figures

List of Tables

Preface

This thesis titled 'Hybrid Force-Position Control of the Motion Compensated Gangway' is submitted for the degree of Master of Science at the Delft University of Technology. The research was conducted under supervision of Dr. Ir. J.W. van Wingerden in the department of Systems and Control at the Faculty of Mechanical, Maritime and Materials Engineering. Daily supervision was given by Ir. J. Koppenol, Lead R&D Engineer at Barge Master B.V.

The project has been carried out during the time span of one year at Barge Master. During this year I was able to carry out a complete design cycle in the field of Systems and Control. From simulation, verification, and validation towards controller design. Finishing off with the actual implementation of my theory at sea, which resulted in a final result to be proud of.

This thesis has been completed with the support of my supervisors, Jan-Willem van Wingerden and Jim Koppenol. Jan-Willem, thank you for the interesting discussions, both on technical level as well as non-technical level. Regardless of the fact that there was good or bad news, you always helped me and left me with new motivation. Jim, Thank you for your continued support during the past year. A lot has changed since we met. I have learned a lot during the time we worked together. Thank you for the technical and moral support. You have shown me how to cross the gap between theory and practice. Furthermore I would like to thank my colleagues at Barge Master and Bosch Rexroth for the cooperation and pleasant working environment.

I would like to thank my family and friends for the much needed distraction and support during the more stressful periods. And finally, Martine, thank you for everything.

Delft, University of Technology — B. Walgaard
November 21, 2017

Chapter 1

Introduction

1-1 Introduction to the offshore industry

The offshore industry can be divided in two mayor fields, the offshore oil and gas industry and the offshore wind power industry. The latter is a fast growing industry which is expected to triple in the coming ten years [7]. For both offshore wind energy as well as oil and gas the lifetime of investments can be divided in three phases. The construction phase, the operation and maintenance phase, and the decommissioning phase. During operation, transportation of personnel and cargo is responsible for a large share of the costs. Wind turbines are often located in areas where high wind speeds are common, high wind speeds result in higher wave heights. Current solutions for transportation suffer from these environmental conditions. Three examples of these solutions are: A swinging basket suspended from a crane (Figure 1-1), crew transfer boats that push against a landing zone (Figure 1-2), and helicopters lowering crew on top of the wind turbine (Figure 1-3). These solutions are highly dependent on weather conditions and become increasingly unsafe with increasing wave heights. The weather windows in which these methods can operate are limited which results in a poor accessibility of the offshore platforms. A decrease in accessibility results in a lower operational efficiency which in turn results in lower revenues. It is therefore favourable to use an access method that can operate during the largest weather window. On top of that, helicopter flights are relatively expensive in comparison to other solutions.

Figure 1-1: Basket on Lewek Falcon. [1]

Figure 1-2: Windcat 10 at monopile. [2]

Figure 1-3: Turbine & helicopter. [3]

The solutions shown in Figure 1-1 to Figure 1-3 all suffer from high winds, high waves, or a combination of both. State of the art solutions in personnel transfer use motion compensation to create a larger operation window. These solutions measure the ship motions and apply actuators to cancel these motions, a cancellation of approximately 95% can be achieved increasing the accessibility of offshore structures significantly. The next chapter will address this technology in more detail.

1-2 Introduction to motion compensation

The objective in motion compensation is to cancel motions at the base using actuators such that the workpiece is stationary. This can be applied to multiple fields. One of the most well known applications is camera stabilization in the film industry, where motions from the camera operator are cancelled to achieve a steady image. In the offshore industry applications vary from drilling, well intervention, pipelay, heavy lifting and personnel transfer. Heave compensation is the simplest form of motion compensation, during heave compensation only the up and down motions of the ship are compensated. Heave motion causes the largest disturbance during deep sea operations such as drilling, deep sea installations or pipelay. Operations such as heavy lifting or personnel transfer requires compensation in more degrees of freedom. During lifting, roll and pitch motions of the ship can introduce swinging motions. For this purpose systems have been designed that compensate in three degrees of motion. Two examples are shown in Figure 1-4 and Figure 1-5. For the purpose of personnel transfer higher standards are required, therefore all ship motions should be taken into consideration when cancelling movements. Ship movement can be defined in six degrees of freedom, three translations and three rotations along the x, y and z axis. These motions will be discussed in more detail in Section 2-2.

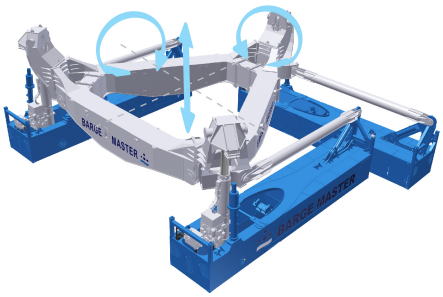

Figure 1-4: Roll-pitch-heave compensated multi purpose platform for 700t loads.

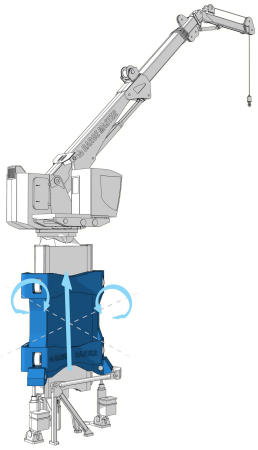

Figure 1-5: Roll-pitch-heave compensated pedestal for mid size cranes.

Control methods in motion compensation

From a high level point of view a control system can be divided in three mayor parts, the sensors, controller, and actuators. For motion compensation, two groups of sensors can be distinguished. The first group measures ship movements. These movements can be measured in multiple ways. For example using optical sensors, global positioning system (GPS), or accelerometers. The latter is used most often for offshore motion compensation. The Motion Reference Unit (MRU) is a sensor unit which combines accelerometers with gyroscopes to determine ship motions in all degrees of freedom. Limitations on MRU sensors are discussed in Section 2-3. The second group of sensors is used to give feedback to the control system. These sensors measure the actual actuator positions. Rotary encoders and linear position sensors are used for this task. The measured movements are used by the controller to determine a setpoint signal for the actuators. Controller structures are implemented in Programmable Logic Controller (PLC) computers which are reliable and redundant, but limited in complexity and computational power. PLC limitations are described in Section 2-5. In the offshore industry, hydraulic actuation is popular due to its high power density [8]. Especially in motion compensation where linear actuation is often required. Hydraulic actuators vary from rotational drives to linear hydraulic cylinders. A high level system structure containing the sensors, controller and actuators is shown in Figure 1-6.

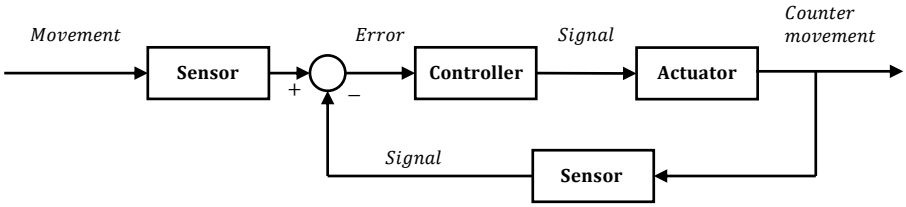

Figure 1-6: High level structure in motion compensation.

1-2-1 Objectives in motion compensation for personnel transfer

The objectives in motion compensation for personnel transfer can be summarized by stating that the objective is to create safe transition from moving object to a different moving or static object. A selection of sub-objectives that can be derived from this objective is to:

- Increase workability
- Measure shipmovement
- Predict shipmovement
- Compensate for shipmovement
- Have a high compatibility with other structures
- Be adaptable to changing environments
- Be fast deployable
- Ensure safety by design

1-2-2 State of the Art in motion compensation

The industry of active motion compensation for personnel transfer is a young industry. The first idea which was the basis for one of the biggest players in the market has been patented in 2004 [9]. The patent filed in 2004 by Ampelmann made use of a Gough-Stewart platform which uses six linear hydraulic cylinders to compensate all six ship motions [10]. Since then multiple competitors have introduced their solution to the problem. Unfortunately, due to the strong competition in the market most research is kept between the walls of the company. A selection of gangway types will be discussed briefly. The company Uptime introduced their gangway in 2012. An aluminium gangway that uses slewing, luffing and telescoping motions for compensation. The same mechanics are used by the gangways introduced by SMST and Kenz Figee Group. A different mechanism is applied by Ztechnologies which has presented a gangway with a pedestal that pivots around two axis at the base combined with a luffing and telescoping motion in the gangway. A completely different design was presented by L-Bow, a containerized gangway system consisting of two hinged telescope sections moving like an shoulder-elbow-hand system.

While the majority of these solutions are still in development, some footage can already be found of working systems. This provides an excellent basis for evaluation. For example, Uptime, Kenz Figee, and SMST use landing cones to provide a steady connection to the offshore structure. When landed using the bumper, slipping motion can be observed [11]. Others use gripper heads to resist the high forces at the tip. This requires a specialized landing zone, for example a landing pole for the Ampelmann O-type [12] or specific boat landing dimensions for the scorpion claws of the Uptime Undertun [13].

Areas for improvement are observed with the mentioned gangways. The Gough-Stewart platform prevents a continuous workflow by having to stop compensation after each transfer. Landing cones add height differences preventing the use of cargo trolleys. Slipping motions reduce safety whereas specialized landing structures are unwanted. The goal of the Barge Master Motion Compensated Gangway is to solve these problems.

1-2-3 Barge Master Motion Compensated Gangway

The Barge Master Motion Compensated Gangway (MCG) uses three actuators to move the tip into the required position. All actuators differ from each other in the sense of working mechanism. The slewing actuator is a rotational drive which acts on a gearbox system to provide rotational movement. The luffing actuator is a linear cylinder which provides a rotational movement through leverage. Finally, the telescope actuator is a rotational drive which provides linear movement through a drum and cable system. Movement directions are shown in Figure 1-7.

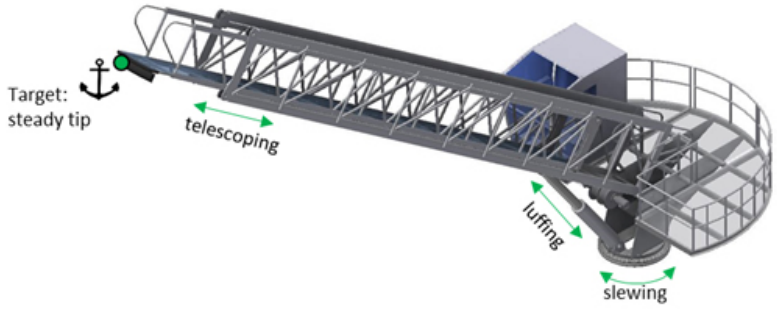

Figure 1-7: Working principle Barge Master Motion Compensated Gangway.

The purpose of the gangway is to keep the tip stationary to facilitate an easy situation where the operator can land the tip on the offshore structure in a safe and accurate way. The operator can use a joystick input to influence the setpoint to the actuators. Slewing luffing and telescoping can be controlled individually by the operator. Compensation can be turned on by the operator prior to landing the tip. After the tip is landed, the connection should be static. In other words, no slip should be present and the tip should not disconnect. No modifications can be made to the landing zone prior to landing, the tip should be able to land and operate on any flat surface. A constant connection is achieved by pressing the tip against the flat service.

When compensation is ideal, the tip will not move with respect to the structure. It will then be easy to generate a constant pushing force. However, in reality this is not the case. An error is introduced by the MRU sensors. MRUs typically suffer from drift in the low frequency region as well as other small measurement errors. This error is multiplied with the tracking error of the position controller. The total position error in the tip relative to the environment causes large forces when the tip is connected to the offshore structure. Therefore a sensor is needed that allows the tip forces to be fed back into the control system. Forces in the system can be obtained using pressure sensors in the actuators or by introducing force sensors in the system. Pressures in the hydraulic system tend to suffer from a range of factors that make this option unsuitable. Friction, hysteresis, stick slip and inertial forces of the gangway cause large variations in the pressure signal. It is therefore necessary to introduce force sensors in the tip of the gangway. A section of the tip will be supported by a set of load pins. Using kinematic relations in the tip structure an approximation of the exact tip force can be made.

1-3 Objective of this thesis

Motion compensation for personnel transfer is a relatively new technology in the offshore industry. Because of the human presence in the system safety is of the highest priority. Unsafe situations can lead to injuries or even death. The area where the risk is the highest is the point of connection to the offshore structure also known as the tip. Therefore a solution has been proposed by Barge Master, the Next Generation Gangway is capable of measuring forces in the tip. Using the tip force measurements all slipping and disconnecting motions can be eliminated. The combination of hydraulic actuation using non-collocated force-position control in an environment with imposed movements is a unique problem. This results in the following research objective:

Design a Hybrid Force-Position controller for the hydraulically driven Motion Compensated Gangway which tracks a tip force setpoint on the environment while performing safely under forced movements.

1-4 Contributions of this thesis

The contributions of this thesis can be summarized in four separate parts. First, the modeling of hydraulic actuators. Second, the application of the model in position control. Third, the design of a force controller that utilizes the position controller as a basis. The fourth part is the application of the designed hybrid force-position control in offshore testing.

1. We have described a model for a **hydraulic actuator** using positions as state variables. In common literature, actuators have been modeled using hydraulic flows and pressures. This change allows for an intuitive approach and describes the actuator as an **ideal velocity source**. This can be used with force, position and velocity measurements in feedback control. The hydraulic model is shown in **Section 3-1**.

2. The actuator model has been used in **position control** and its performance is shown in a 3d model. Position control with feedforward was capable of eliminating approximately 95% of the ship motions. When connected to the environment, the **residual motions** generated **force variations as high as 50kN**. These forces will generate slipping motions and loss of contact is expected. The results of the simulation are shown in **Section 3-4**.

3. We have shown that using a force measurement to control an ideal velocity source benefits from integral action. The position control loop has been extended with an outer **proportional-integral force control** loop. The proposed controller structure showed a **reduction the force variations with 95%**. The design of the hybrid force-position controller is discussed in **Chapter 4**.

4. The hybrid force-position controller has been implemented in the motion compensated gangway and **tested at sea**. This showed a significant improvement in performance. Force variations were approximately 20% higher than modeled, this can be attributed to unmodeled disturbances and sensor noise. **A force variation of 1.4kN** was achieved which was acceptable. The connection to the offshore structure was stable and **no slip** occurred. The results of the sea trials are shown in **Chapter 5**.

1-5 Thesis organization

In order to design a fully functional hybrid force-position controller a few steps should be taken. The system with its limitations and the requirements will be discussed in Chapter 2, after which the basis control structures are analyzed in Chapter 3. This basis will be used by the force controller that is designed in Chapter 4. Finally, the results and conclusions are presented in Chapter 5 to Chapter 6.

Chapter 1 - Introduction gives an overall introduction on the market and the environment in which the Barge Master Gangway operates. The objectives and state of the art in motion compensation are introduced together with a general introduction of the Barge Master Gangway. After which the objective of this thesis is defined. Finally the contributions of this thesis are summarized.

Chapter 2 - System Description starts with a more technical focused introduction of the gangway. An explanation on the differences between free floating and landed control is given. The basics are introduced. Reference frames, actuator degrees of freedom as well as the available inputs and outputs for motion compensation are discussed. Followed by the design considerations and requirements that have been the basis for design choices earlier in the process.

Chapter 3 - Preliminaries for Position Control shifts the focus towards the technical details relevant for control. Before the gangway lands on the offshore structure it will be in position control. Therefore position control serves as a basis for the final control structure. All relevant subjects will be discussed in this chapter. A model is presented for hydraulic actuation. The method for determining actuator setpoints as well as feedforward control is treated in detail. Finally, the performance of the position controller is simulated using a 3D model.

Chapter 4 - Force Control starts with the introduction of a tip stiffness through which the tip is connected to the environment. Residual motions in the tip generate tip forces which influence the dynamics. A dynamic analysis in 1D is done after which controller structures are proposed and analyzed. Proportional and proportional-integral controllers are analyzed by closing the loop using the root locus method. An intuitive representation of the force feedback to an ideal velocity source is used to justify the integral action.

Chapter 5 - Results discusses the results obtained during sea trials. Two controller structures have been implemented in the software of the gangway and put to the test during offshore testing. The expected instability and lack of performance is observed in one controller structure. The solution performed as expected and provided stability.

Chapter 6 - Conclusion and recommendations presents the conclusions that can be drawn from the modeling and design of the hybrid force-position controller. The chapter is closes with recommendations for further research.

Chapter 2

System Description

This chapter will present the overall layout of the system and its operational modes. The reference frames which are relevant for motion compensation and the degrees of freedom in which the gangway can move are shown. Then, the design considerations are discussed. The characteristics of ship movements and how the motion sensors behave to these motions are discussed. The requirements for the landing zone and the corresponding tip forces are presented as well as limitations on the complexity of the controller structure. Furthermore, a short explanation of the role of the operator is given.

2-1 Barge Master Motion Compensated Gangway

In the field of motion compensation all systems move with respect to each other. Therefore it is of great importance to start with a clear definition of reference frames. The reference frames will be used to express motions and locations of the system with respect to itself and the earth. The four most important reference frames used are shown in Figure 2-1. The earth reference frame (Ψ_e) is an inertial frame fixed at an arbitrary point in space. The Motion Reference Unit (MRU) reference frame (Ψ_{MRU}) is fixed with the ship location, ideally in the center of mass of the ship. The ship's movements are defined as a relative motion between frame Ψ_e and Ψ_{MRU}. The Motion Compensated Gangway (MCG) reference frame (Ψ_0) is fixed at the base of the gangway pedestal and will not move in the MRU reference frame. Finally, the gangway tip reference frame (Ψ_3) is fixed in the tip. The tip reference frame is to be kept stationary in the earth reference frame using actuators in the gangway.

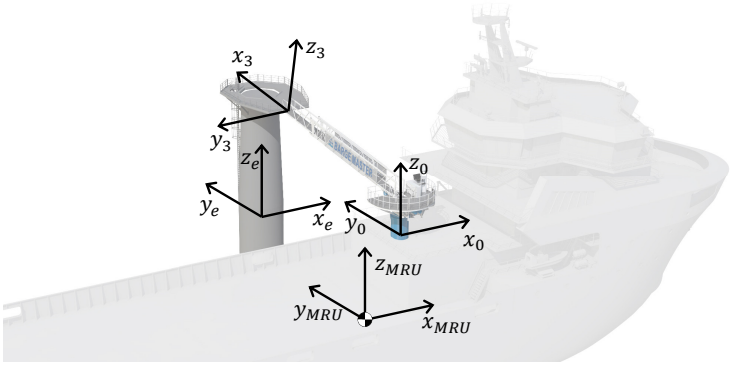

Figure 2-1: Definition of four basic reference frames used in gangway model.

Three hydraulic actuators facilitate movement between the base reference frame and the tip reference frame. The actuators form an open kinematic chain with rotation in the horizontal plane, rotation in the vertical plane, and linear movement of the gangway. These actuator movements are referred to as slewing, luffing, and telescoping respectively with measured positions represented by the state variables $q = [\, q_1 \quad q_2 \quad q_3 \,]^T$. The workspace represents the collection of reachable tip locations in the base reference frame. The workspace is shown in Figure 2-2.

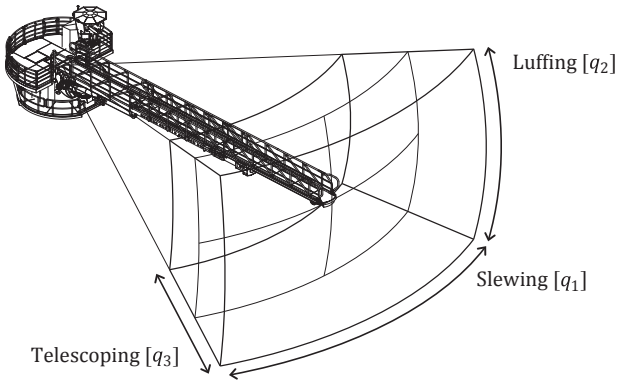

Figure 2-2: Degrees of freedom and workspace in which the gangway operates.

The gangway will be used during two different control cases. The first case is free floating position control. During position control the objective is to regulate the tip motionless in the earth reference frame. The second case is when the gangway is landed against an offshore structure fixed in the earth reference frame. In both cases the position and movement of the defined reference frames should be determined. This is achieved by measuring the ship movements using an MRU. The location of the tip is determined by measuring the positions of the actuators. During the landed phase no tip forces are present when position control is perfect. However, in reality, this is not the case. Therefore, tip forces are measured in x, y, and z direction. These signals can be used for control. The valves of the hydraulic actuators

are controlled by a voltage, the voltage is linearly dependent with the hydraulic flow. These are the only signals that can be used by the control system to influence the system. An overview of the available signals is given in Table 2-1.

Table 2-1: List of variables available for position and force control.

Case	Control	Inputs	#	Outputs	#
Compensation	Position	Valve setpoint	3	Ship position & velocity	12
				Actuator positions	3
Tip landed	Force-Position	Valve setpoint	3	Ship position & velocity	12
				Actuator positions	3
				Tip forces	3

2-2 Ship movement

Wave motions are highly unpredictable, however, an accurate approximation can be made by a representation of waves that consists of a spectrum of linear waves. Well known spectra are the Pierson-Moskowitz spectrum [14] and the JONSWAP spectrum [15]. These spectra can be scaled to a certain significant wave height (H_{sig}), which is defined as four times the standard deviation of the surface elevation [16].

The response of the ship to a wave spectrum is represented by a set of transfer functions also known as response amplitude operator (RAO)s. The RAOs contain a magnitude and phase response for the wave frequencies and angles from which the waves hit the ship. Using the wave spectrum and the RAOs, ship motions can be estimated. Movements in six degrees of freedom, three translations and three rotations are defined in Figure 2-3.

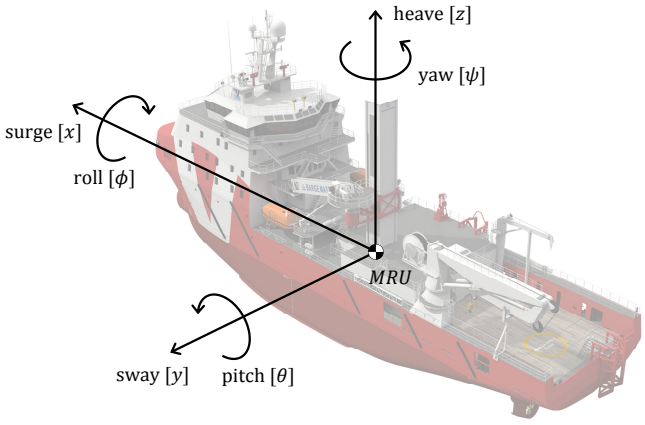

Figure 2-3: Definition of the vessels degrees of freedom. [4, 5]

RAOs can be obtained by computational fluid dynamics (CFD) simulations or by scale model tests in simulated wave tanks. For this project, a data set containing movements of a compa-

rable sized ship is used. These time traces are obtained from scale model tests with simulated wave motions. Motion data of the first three minutes is shown in Figure 2-4. This dataset is generated with a H_{sig} of $2.5m$ and a wave heading of 225 degrees [4].

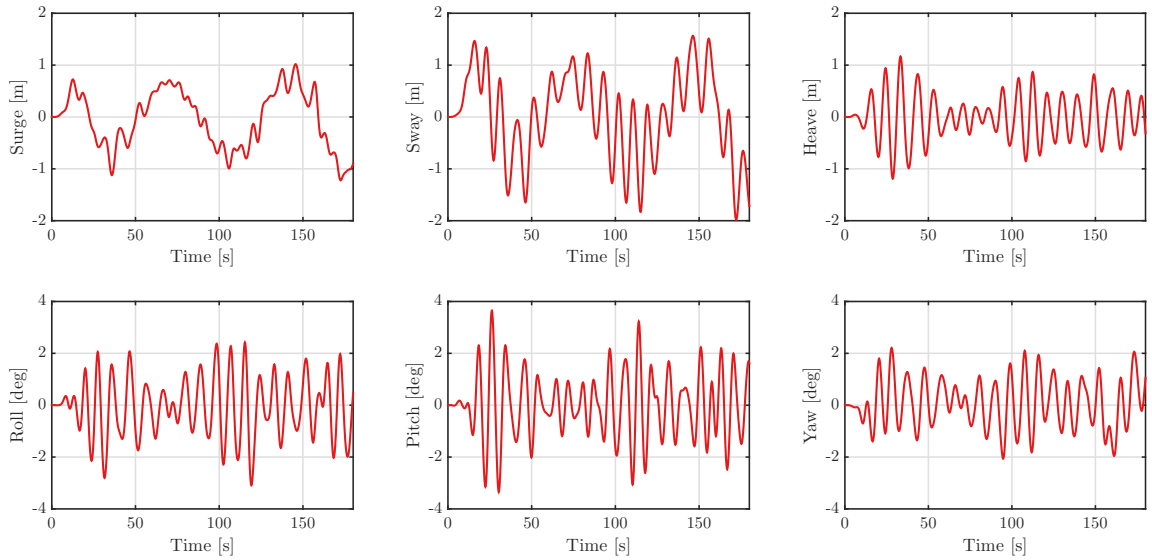

Figure 2-4: First three minutes of ship movements in six degrees of freedom.

Notice that the surge and sway signals in Figure 2-4 contain a low frequency and a higher frequency component. The low frequency component will not be observed by the MRU sensors, this effect will be discussed in the next section.

2-3 MRU characteristics

An MRU, also referred to as an Inertial Measurement Unit (IMU), uses accelerometers and gyroscopes to measure its location and orientation. By measuring acceleration the signal is integrated to obtain the location data. A small acceleration signal error can result over time in a large position error. High pass filters are applied to compensate for this problem. The result of this solution is that low frequency movements will not be observed. As shown in Section 2-2 the surge and sway movements contain low and a high frequency components with periods of approximately 60 seconds and 10 seconds. The low frequency movement will not be observed by the MRU, the power spectral density (PSD) of the shipmotions and the shipmotions observed by the MRU are shown in Figure 2-6. The unobserved motions in the time domain are shown in Figure 2-5. It is expected that this error will not give problems during position control. The error dynamics are very slow and can be accounted for by the operator during position control. However, during the landed scenario, this error can generate large tip forces which need to be controlled [17].

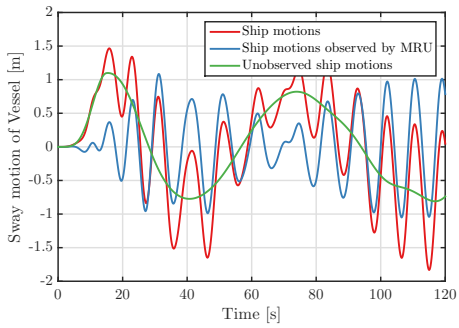

Figure 2-5: Time domain comparison of actual and observed sway movements by MRU.

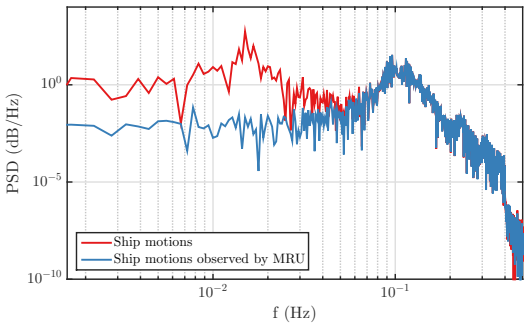

Figure 2-6: PSD of actual and observed sway movements by MRU.

2-4 Landing zone

Landing the gangway tip by clamping or hooking on a structure needs a specific modification of the landing zone. This is a costly process and not always possible. The Barge Master Gangway increases accessibility by using a solution that relies on friction. Using friction allows the tip to be landed on any flat surface, see Figure 2-7. By pushing a rubber bumper tip against the landing zone, friction will not cause the tip to slip. Residual motions generate forces in z and y direction, see Figure 2-8.

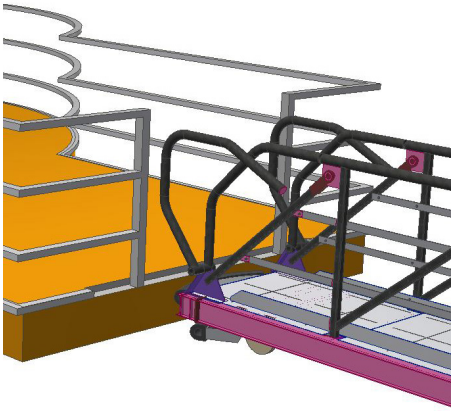

Figure 2-7: Tip landing zone at wind turbine.

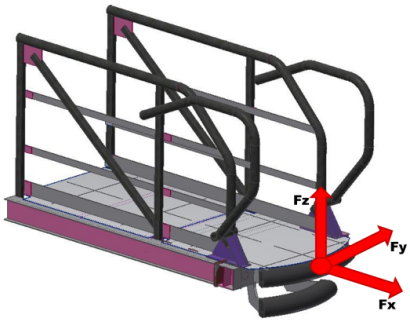

Figure 2-8: Definition of forces in tip.

Slip occurs if these in-plane forces exceed the maximum friction force. Therefore a sufficient pushing force is required. The landing zone should be designed for these forces. Tip forces will be actively regulated by the control system. The force setpoints and their controlled error requirements are shown in Table 2-2 [18]. During operations and landing, impact forces can exceed these values. Therefore a design force is given for the landing zone. In the highly unlikely event of a redundancy failure, higher forces can occur. These limit forces are also shown in Table 2-2.

Table 2-2: Tip target forces, acceptable forces during compensation and structural design forces.

	Target [kg]	Max [kg]	Design force [kg]	MCG Limit [kg]
F_x	400-800	800	2000	6500
F_y	0	160	400	5500
F_z	0	160	400	4500

2-5 PLC control

The actuator valves are controlled by the Programmable Logic Controller (PLC) computers. These industrial computers are rugged and reliable in harsh environments. Although PLC computers can be used for complicated control systems [19], the computational power still lacks in comparison to PCs. Furthermore, for future servicing and problem solving it is important to avoid complex controller structures.

Each actuator is controlled by a specific PLC controller referred to as a Hydraulics-capable NC Control (HNC) computer. HNCs accept a position and a velocity setpoint. Feedforward and PID-feedback is possible in the HNC structure. The HNC controls the voltages send to the actuator valves. Due to different piston areas in the actuators flows have a nonlinear relation for positive and negative movement, these differences are compensated for by the HNC.

2-6 Operator input

The operator is responsible for landing the gangway to the structure. This is done using joysticks to control the three actuators separately. A joystick input corresponds to a velocity setpoint on an actuator. The integral of the velocity setpoint is added to the position setpoint. When in compensation mode, these joystick velocity and position setpoints are added to the MRU velocity and position setpoints. Higher level control such as ramps, limiters and if-then-loops are applied to the joystick signal but this will not be part of the scope of this thesis.

In this chapter the general control scenarios and purpose of the gangway have been described. High level design considerations have been discussed. These factors will be taken into consideration during control design. the next chapter will treat the position control in more detail. Position control is the basis on which the force control is designed and will be active even during the landed scenario.

Chapter 3

Preliminaries for Position Control

During compensation mode no external forces are present and the gangway will operate in position control. The MRU position and velocity signals are transformed to a tip position and velocity setpoint using the axis transformations, an overview of the reference frames is shown in Figure 3-2. The actuator setpoints are determined using inverse kinematics. Then, a simple loop is closed to facilitate position control on actuator level. The actuator velocity setpoint will directly be used as input for the actuator valves, also known as feedforward. The layout of the position control scheme is shown in Figure 3-1. Here, $\dot{q}_{act}$ is the actuator valve velocity setpoint. The actuator valve bandwidth is sufficiently high as such that they can be assumed ideal. The characteristics of hydraulic actuation are discussed in depth in Section 3-1.

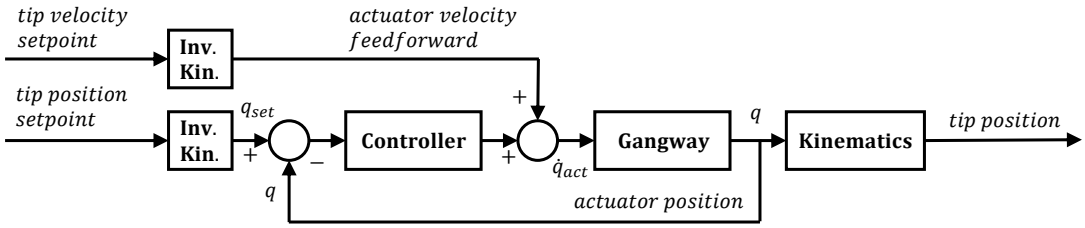

Figure 3-1: Block diagram for gangway in position control.

The tip position and tip velocity setpoints should ideally represent a fixed point in the earth reference frame. In reality this is not the case. An error is introduced by the Motion Reference Unit (MRU) sensors. MRUs typically suffer from drift in the low frequency region as well as other small measurement errors. This error is multiplied with the tracking error of the position controller. The total position error in the tip relative to the environment causes large forces when the tip is connected to the offshore structure. The layout of the system with the tip landed is discussed in Chapter 4.

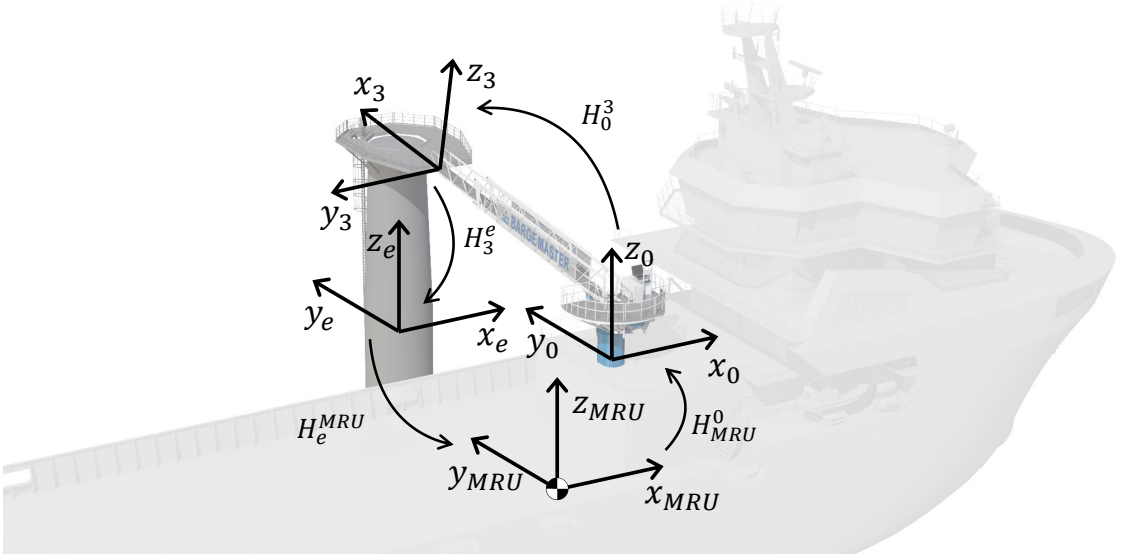

Figure 3-2: Overview of reference frames with corresponding transformation matrices.

3-1 Hydraulic actuation

Hydraulic actuators can be seen as power converters from one physical domain to the other. A hydraulic actuator transforms a hydraulic flow into a translational or rotational movement. See Table 3-1 for the relations between the power variables.

Table 3-1: Physical domains in hydraulic actuation.

Physical domain	Flow	Effort
kinetic hydraulic	pressure	volume flow
kinetic translation	force	velocity
kinetic rotation	torque	angular velocity

The volume flow is controlled by solenoid actuated valves. These valves operate at a bandwidth of approximately 50Hz and can be assumed not to limit the performance of the system. Hydraulic power is provided by the hydraulic power unit (HPU) which can provide a flow of approximately 400 liters per minute at a pressure of 260 bar. At peak performance, the required power will not exceed the maximum power output of the HPU. Therefore it is safe to assume that when a flow setpoint is given to the valve it will be realized instantly. Valves are controlled by Hydraulics-capable NC Control (HNC) computers which will compensate for differences in cylinder areas or rotational drive stroke volumes such that the input voltage is linearly related to the achieved actuator velocity. It is sufficiently accurate for the purpose of this thesis to assume that the valves work as ideal velocity sources. In literature, hydraulic actuators are often modeled with flows as inputs. For the application in HNC controlled actuators, a simplified model of a bottom driven hydraulic actuator provided by Bosch Rexroth (BRR) is rewritten to a model with velocity input.

The simple model that has been provided by BRR is shown in Figure 3-3. In this model the

valve setpoint is represented as a flow Q provided to the actuator. The outputs of the model are the pressure p and the mass position q.

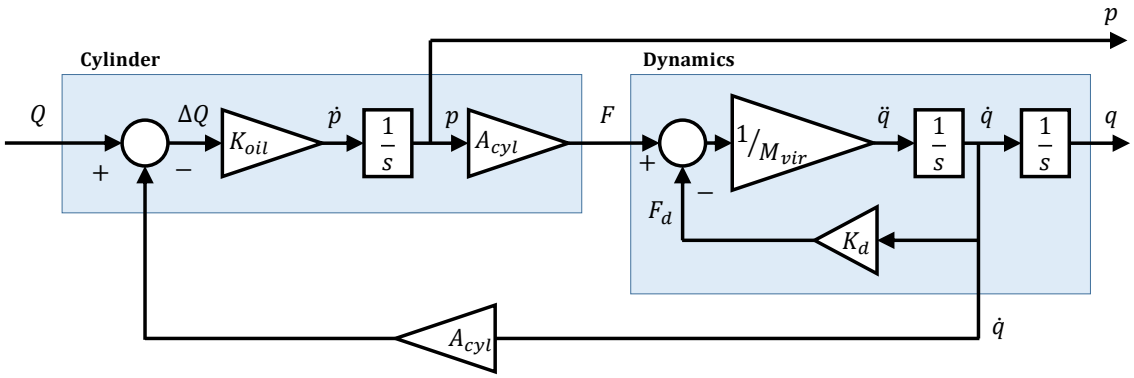

Figure 3-3: Hydraulic model of a cylinder with added friction, as provided by BRR.

The increase in pressure in the cylinder is determined by the increase of provided oil minus the extension of the cylinder times the cylinder area. This increase of volume is multiplied with the oil constant K_{oil}, which is defined for a bottom driven actuator as:

$$K_{oil} = \frac{E_{oil}}{A_{cyl} q_{max} + V_L} \tag{3-1}$$

The equation for the oil constant uses the maximum stroke q_{max} and the volume of oil in the piping V_L. By using q_{max} the model is linearized at the lowest stiffness, this is a conservative assumption. No dissipation was present in this model. Dissipation can be added as damping to achieve a more realistic model.

Three integrators are present in this model, and thus this model can be represented by a state-space model with three states. This is shown in Eq. (3-2) and Eq. (3-3).

$$\begin{bmatrix} \dot{q} \\ \ddot{q} \\ \dot{p} \end{bmatrix} = \begin{bmatrix} 0 & 1 & 0 \\ 0 & -\frac{K_d}{M_{vir}} & \frac{A_{cyl}}{M_{vir}} \\ 0 & -A_{cyl} K_{oil} & 0 \end{bmatrix} \begin{bmatrix} q \\ \dot{q} \\ p \end{bmatrix} + \begin{bmatrix} 0 \\ 0 \\ K_{oil} \end{bmatrix} Q \tag{3-2}$$

$$\begin{bmatrix} q \\ p \end{bmatrix} = \begin{bmatrix} 1 & 0 & 0 \\ 0 & 0 & 1 \end{bmatrix} \begin{bmatrix} q \\ \dot{q} \\ p \end{bmatrix} \tag{3-3}$$

The model proposed by BRR uses the oil constant and a set of states that makes analysis of the dynamics too abstract. A change in states is proposed for application with the HNC contolled ideal velocity valves. This change helps to make the model more intuitive to understand in physical terms. The model can be represented by a mass spring damper system as shown

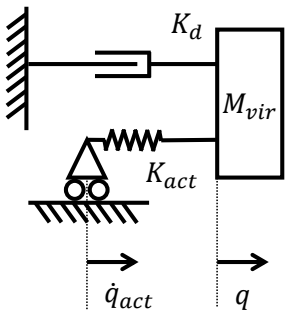

Figure 3-4: Free body diagram of the desired simplified model.

in Figure 3-4. The $\dot{q}_{act}$ value is determined by the oil flow. K_{act} is determined by the relation between force on the cylinder and displacement. K_{act} is often given in literature, both for linear and rotating hydraulic actuators. Then, in block scheme, the model is shown in Figure 3-5. The state space form of the model is given in Eq. (3-4) and Eq. (3-5). This

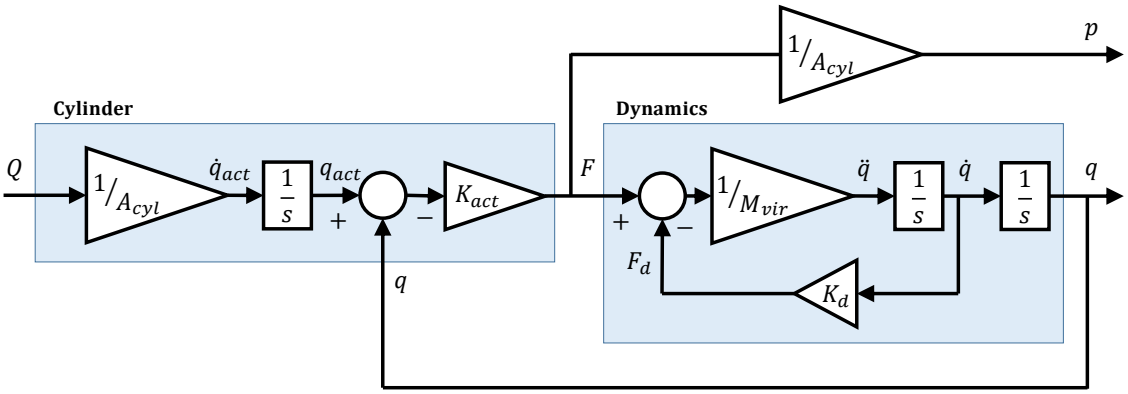

Figure 3-5: The edited hydraulic model of a cylinder with friction.

model uses the same input and outputs as the original model. The third state has changed from pressure to the setpoint position of the actuator. The A-matrix resembles a mass damper

spring system more closely.

$$\begin{bmatrix} \dot{q} \\ \ddot{q} \\ \dot{q}_{act} \end{bmatrix} = \begin{bmatrix} 0 & 1 & 0 \\ -\frac{K_{act}}{M_{vir}} & -\frac{K_d}{M_{vir}} & \frac{K_{act}}{M_{vir}} \\ 0 & 0 & 0 \end{bmatrix} \begin{bmatrix} q \\ \dot{q} \\ q_{act} \end{bmatrix} + \begin{bmatrix} 0 \\ 0 \\ \frac{1}{A_{cyl}} \end{bmatrix} Q \tag{3-4}$$

$$\begin{bmatrix} q \\ p \end{bmatrix} = \begin{bmatrix} 1 & 0 & 0 \\ -\frac{K_{act}}{A_{cyl}} & 0 & \frac{K_{act}}{A_{cyl}} \end{bmatrix} \begin{bmatrix} q \\ \dot{q} \\ q_{act} \end{bmatrix} \tag{3-5}$$

This model can be reduced to a model with input $\dot{q}_{act}$. The internal force of the actuator can be chosen as an output, which completely drops the cylinder area A_{cyl} from the equation. The simplified model with the correct states, in, and outputs can be applied to the three actuators of the gangway. The final simplified actuator model is shown in Figure 3-6, the frequency response is shown in a bode plot in Figure 3-7. The telescope actuator has a gain margin of 32.2 dB and a phase margin of 86.6 degree. In the following subsections the three actuators that are used in the gangway are discussed in more detail.

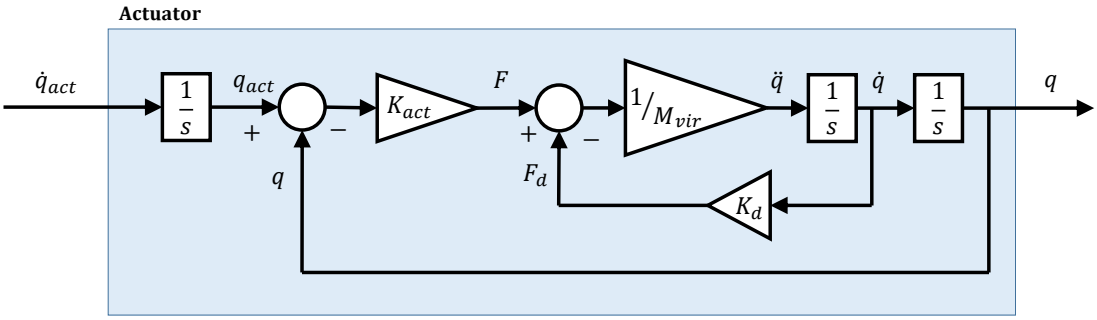

Figure 3-6: Final simplified actuator model of hydraulic cylinder with dynamics.

Slewing actuator

The slewing actuator consists of multiple rotational drives working on a large slewing ring. There is no backlash present between the pinions and the slewing ring. Hydraulic rotational motors demonstrate the same dynamics as hydraulic cylinders. With a linear rotational stiffness and a factor which relates rotational speed to flow. A graphical impression of the hydraulic motor assembly is given in Figure 3-8. The slewing motors are two double drive rotational motors connected in series. This produces a stiffness as shown in Eq. (3-7). The transmission consists of a gearbox and a pinion which drives the slewing ring. The calculation

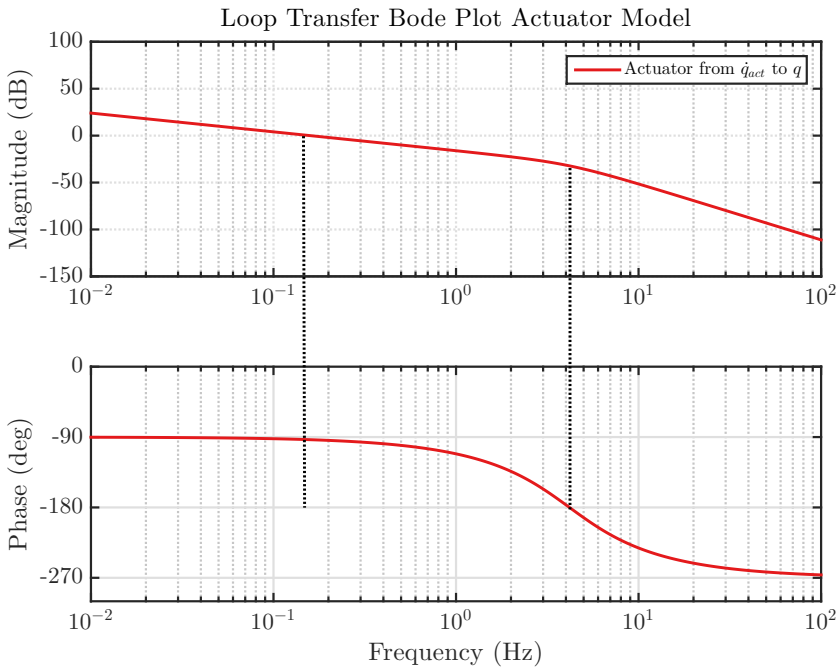

Figure 3-7: Bode plot of the simplified actuator model, parameters of the telescope actuator are used.

of the stiffness which acts on the slewing ring is shown below.

$$K_{oil} = \frac{4E_{oil}}{\pi V_{g_{slew}} + V_L} \tag{3-6}$$

$$K_{motor} = \frac{4E_{oil}V_{g_{slew}}^2}{\pi V_{g_{slew}} + V_L} \quad (\mathrm{N\,m\,rad^{-1}}) \tag{3-7}$$

$$K_{act} = \frac{4E_{oil}V_{g_{slew}}^2(i_{gear}i_{pin})^2}{\pi V_{g_{slew}} + V_L} \quad (\mathrm{N\,m\,rad^{-1}}) \tag{3-8}$$

Luffing actuator

For the luffing cylinder, a double driven cylinder is used. Which means that both chambers in the cylinder are pressurized and connected to the valves. With the oil flow controlled to both chambers, double driven actuators can exert pushing and pulling forces on the environment. However, the double driven cylinder was not chosen for this reason. A double driven actuator is used because it has a significantly higher stiffness than bottom end driven cylinders. Both chambers act as parallel springs which causes a stiffness curve with an approximately constant stiffness in the working area. See Figure 3-10. Therefore, the assumption of a constant stiffness can be made.

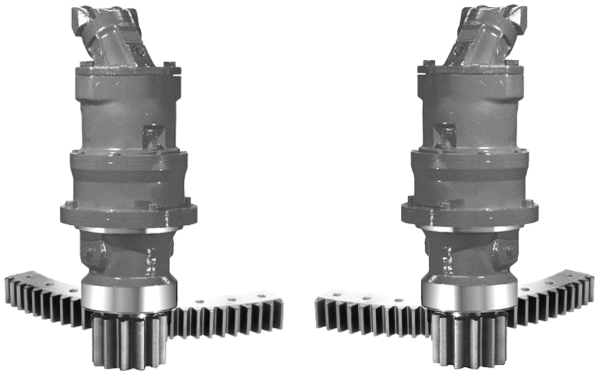

Figure 3-8: Two hydraulic rotational motors with gearbox and pinion acting on a slewing ring.

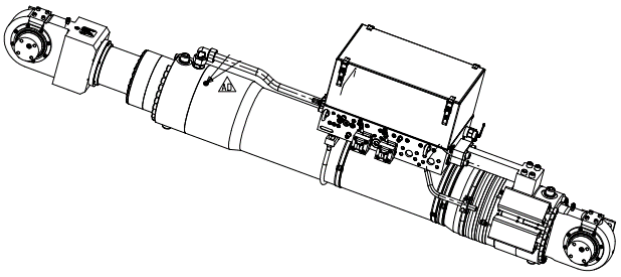

Figure 3-9: Luffing cylinder.

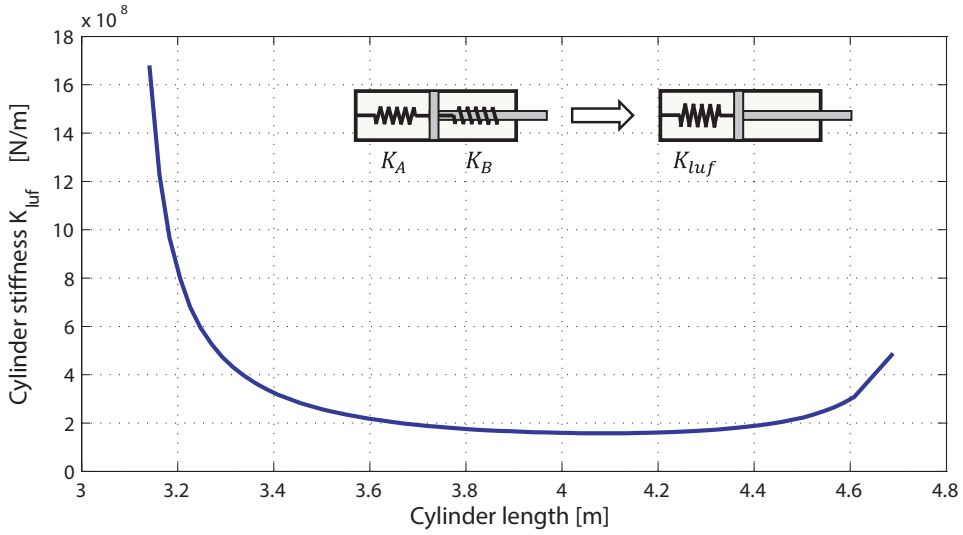

Figure 3-10: Equivalent total stiffness K_{luf} for double acting luffing cylinder.

Telescope actuator

The second telescope is driven by a direct drive hydraulic motor. The motor drives a winch drum which connects to the telescope with a cable. The winch drum translates the rotational

motion of the motor to a linear motion of the cable and the telescope. The telescope winch is shown in Figure 3-11 and the linear motion of the gangway shown in Figure 3-12. Both

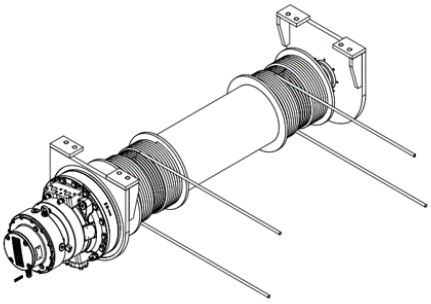

Figure 3-11: Telescope winch.

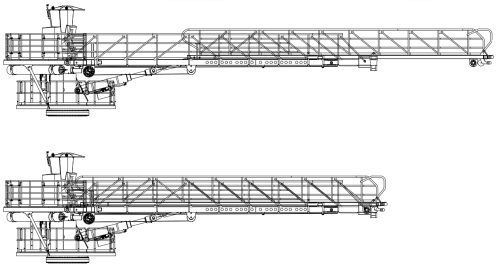

Figure 3-12: Telescope extension using a cable system.

the hydraulic motor and the cable behave as springs, the reflective spring constant on the telescope is calculated as shown below.

$$K_{winch} = \frac{4E_{oil}V_{g_{winch}}^2}{R^2(\pi V_{g_{winch}} + V_L)} \quad (\mathrm{N\,m^{-1}}) \quad (3\text{-}9)$$

$$K_{act} = \frac{1}{(1/K_{winch} + 1/K_{cable})} \quad (\mathrm{N\,m^{-1}}) \quad (3\text{-}10)$$

3-2 Neutral Setpoint

Position control will be achieved by using a fictitious point in space which is the goal for the tip position. When compensation is off, the neutral point will coincide with the actual tip location. The location of the tip in the gangway reference frame will be determined using the actuator angles, see Figure 3-13a. The location of the gangway in the MRU reference frame is known and will not change during operation. Therefore, the tip location in the MRU frame is known when all actuator angles are known. See Figure 3-13b Activation of compensation mode makes a snapshot of the current tip location and locks it in the earth reference frame, this will be the neutral point. Then, shipmotions are measured by the MRU. The MRU signals can be used to determine the location of the ship relative to the earth. By knowing the position of the MRU in the earth reference frame, the location of the neutral point is known in the MRU and gangway reference frame. See Figure 3-14a. Finally, by knowing the degrees of freedom of the gangway, corresponding actuator angles can be determined using inverse kinematics. See Figure 3-14b.

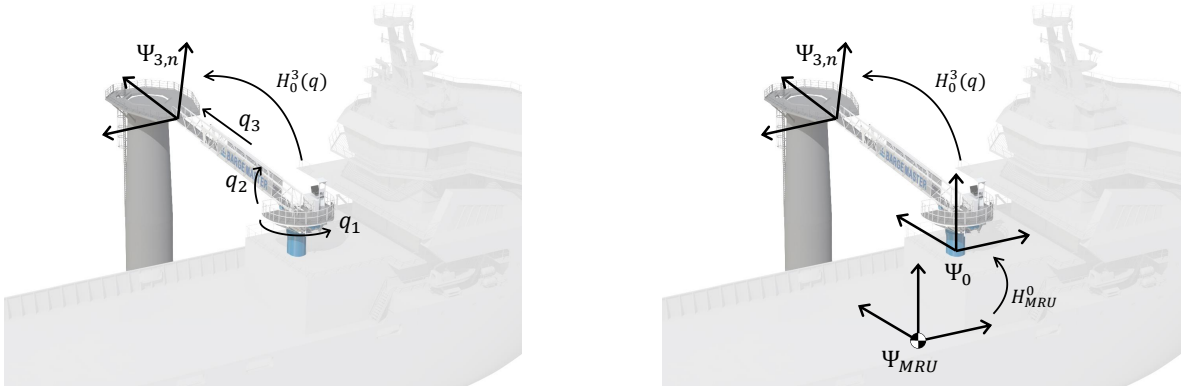

(a) Kinematics **(b)** Tip location in MRU reference frame

Figure 3-13: Kinematics are used to determine the tip location, this is related to the MRU reference frame

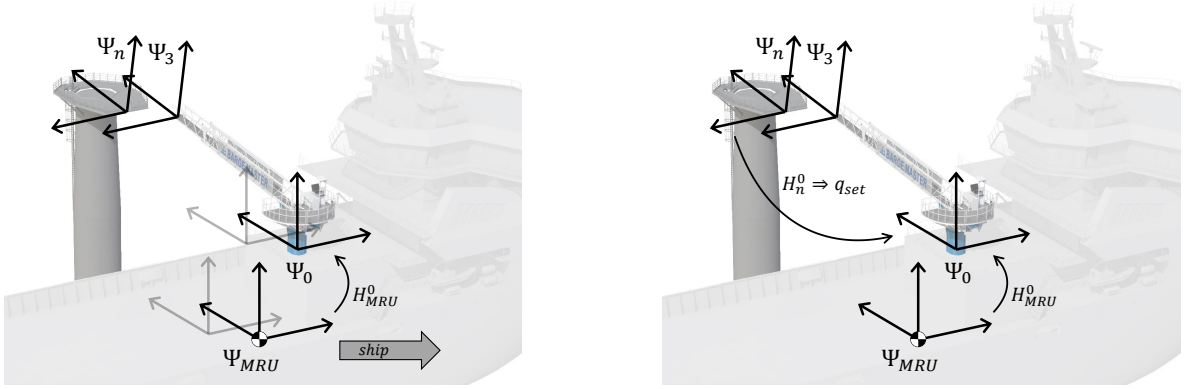

(a) Neutral setpoint after movement **(b)** Inverse kinematics

Figure 3-14: After movement, neutral setpoint separates from tip location and desired actuator angles are determined using inverse kinematics

3-3 Feedforward control

As seen in Figure 3-1, a feedforward controller is present during position control. The feedforward component has a substantial effect on the performance. This will be shown in this section by rewriting the block diagram such that the actuator setpoint acts as a disturbance. Figure 3-15 shows the controlled actuator from Figure 3-6.

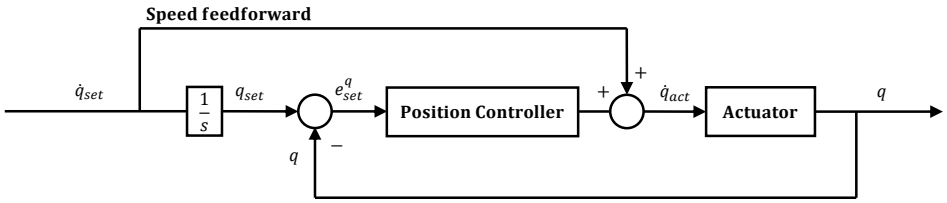

Figure 3-15: Speed feedforward applied on the simple actuator model.

In Figure 3-16, the block diagram has been rearranged such that q_{set} enters as a disturbance. The setpoint is a zero error on the actuator position. Now, the feedforward signal can be taken out of the loop as shown in Figure 3-17. This shows that the feedforward action only influences the zeroes of the system transfer functions and thus no stability issues should be expected from the feedforward controller.

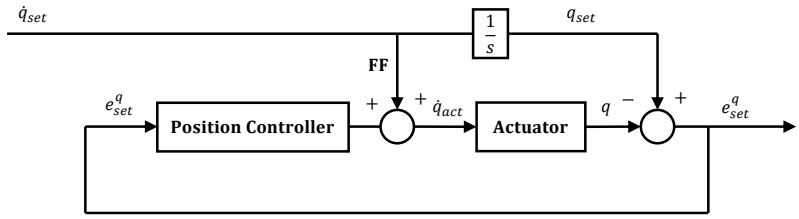

Figure 3-16: Simple position controlled actuator model rewritten with q_{set} as disturbance..

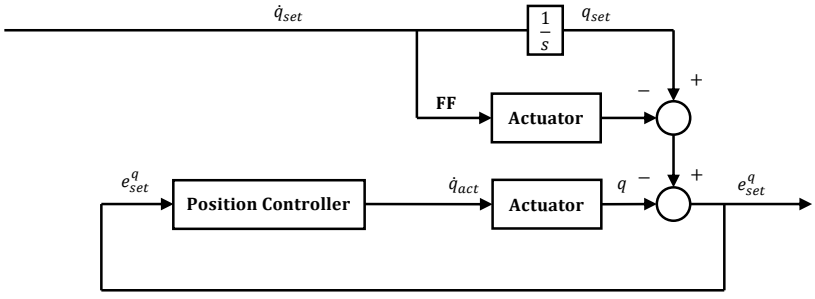

Figure 3-17: Simple position controlled actuator model with the feedforward signal isolated.

An estimation can be given on the percentage of ship motions that can be cancelled using only feedforward. By using the parameters for the telescope actuator given in Section 3-1 with a telescope mass of 2454 kilogram. A power spectral density (PSD) of the shipmotions

in the direction of the telescope actuator can be multiplied with the transfer function from the actuator setpoint to the actuator setpoint after feedforward compensation. The PSD of the ship motions is normalized to a 3σ motion of 1 meter. The feedforward compensation is capable of reducing the motions by 95% to a residual motion of 5 cm. This can be seen in Figure 3-18.

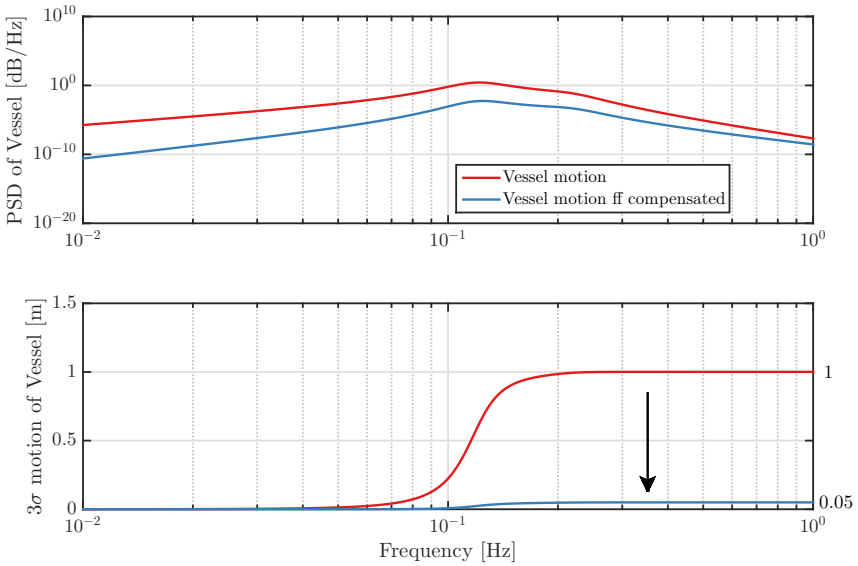

Figure 3-18: Uncontrolled and feedforward compensated vessel motions in the tip.

3-4 3D model

The 3D model has an investigative purpose. Up to this point all individual components of the gangway system have been sized and calculated. It is still unknown whether there are any unforeseen interferences between the systems. It is too expensive to build a complete prototype, and thus simulations can give valuable data about the complete functioning of the system.

- Identify possible problems.
- Validate linear approximations.
- Give confidence in complete functioning of the system.

This project focuses on the tip error during position control and the tip forces when the tip is connected to the offshore structure. However, all state parameters shown in Figure 3-20 can be extracted from the simulation. Furthermore, force step inputs can be given on the tip and the operator can give a velocity setpoint to the actuators using a joystick. This velocity setpoint will be added to the velocity setpoints calculated by the position and force controllers. The model accepts two ship motion channels, the first is the actual ship motions which affect the dynamics, and the second is the ship motions perceived by the MRU. Allowing a distinction

between the low frequency movements and the high frequency movements defined in Section 2-3.

3-4-1 Kinematics and Dynamics

The Motion Compensated Gangway uses three actuators which form an open chain mechanism. The actuators are located such that the tip can be moved in the three translational degrees of freedom. This set up allows us to model the Gangway as a robotic arm. Kinematic relations are determined using screw theory which results in the geometrical Jacobian. The Jacobian plays an important role in the relation between tip velocities and actuator velocities. Likewise the inverse is true for tip forces and actuator forces. These relations are described in Appendix A. Using the kinematic relations, the dynamic relations are derived using the Euler-Lagrange equations, see Appendix B. Furthermore, ship dynamics have been added to the model by placing it in a non inertial frame of reference (Appendix B). An approximation is made of the first two eigenmodes of the lateral deflection in both horizontal and vertical direction of the telescope, these derivations can be found in Appendix C. In position control an approximation can be made of the residual tip motions. Tip forces can be derived by connecting the tip to the offshore structure with a spring.

3-4-2 Model Layout

The model consists of two parts, one offline generation script which creates model matrices and kinematic relations as function of the system states. And the simulation script which runs the functions created by the first script at 100 Hz. The parameters that are used for the offline generation of the matrices are shown in Figure 3-19 represented by ovals. The functions that are created by the script are indicated by rectangles with double-struck vertical edges. These are called by the simulation script. The flow of the simulation script is shown in Figure 3-20. Here, the initial conditions and the actuator properties can be changed. Parallelograms indicate vectors with variable state parameters or predefined vectors such as ship motions or setpoints.

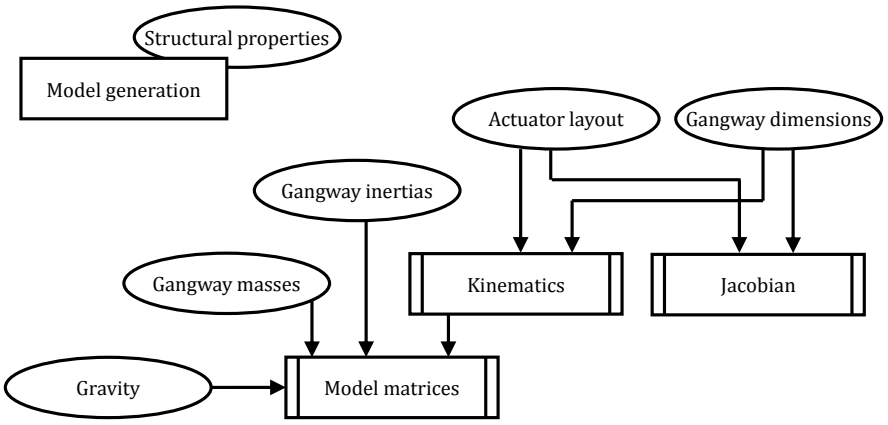

Figure 3-19: Offline generation of model matrices, kinematics and Jacobian.

3-4-3 Results of the 3D model

A few examples of the results from the 3d model are shown in this section. The first two figures show the performance in position control. Figure 3-21 shows the individual tip errors and Figure 3-22 shows the norm of all the errors. The position controller performs better than expected before, with a position error of 4 cm.

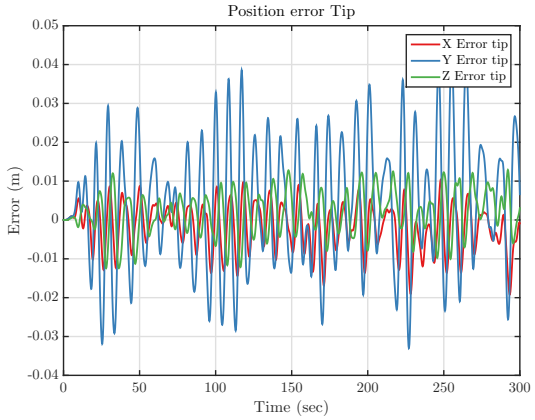

Figure 3-21: Simulated tip position errors during position control.

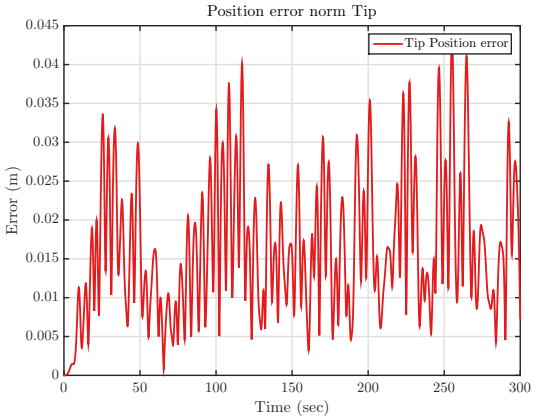

Figure 3-22: The norm of the simulated tip position errors during position control.

Next, the tip is connected to the offshore structure through a flexible tip. The tip forces influence the tip motions, the tip errors have been reduced, see Figure 3-23. However, the tip forces are very large, especially for the compression force in x direction. See Figure 3-24. An average tip force variation of 4000 Kg is present. This is unacceptable and does not fulfill the requirements defined in Section 2-4. Therefore, a solution using tip force feedback control should be implemented. The analysis and design of the force controller is the subject of the next chapter.

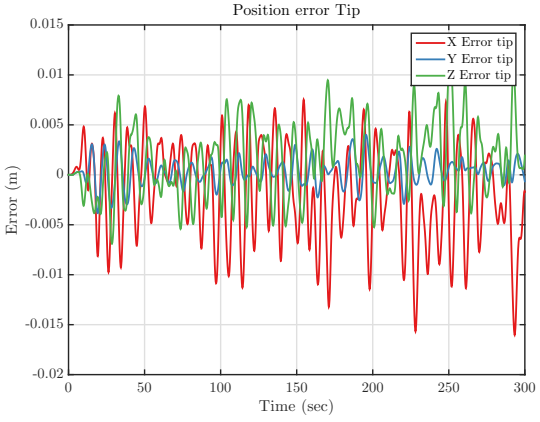

Figure 3-23: Simulated tip position errors during position control with the tip connected.

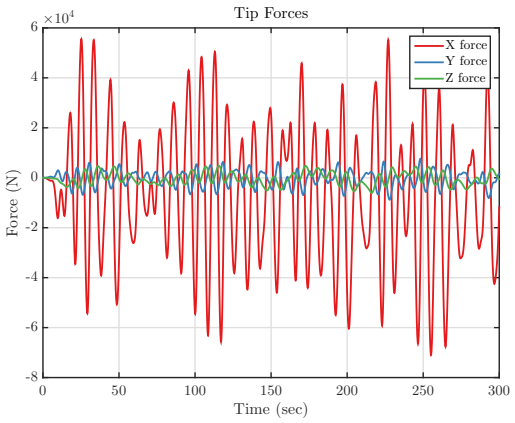

Figure 3-24: Simulated tip forces during position control without force control.

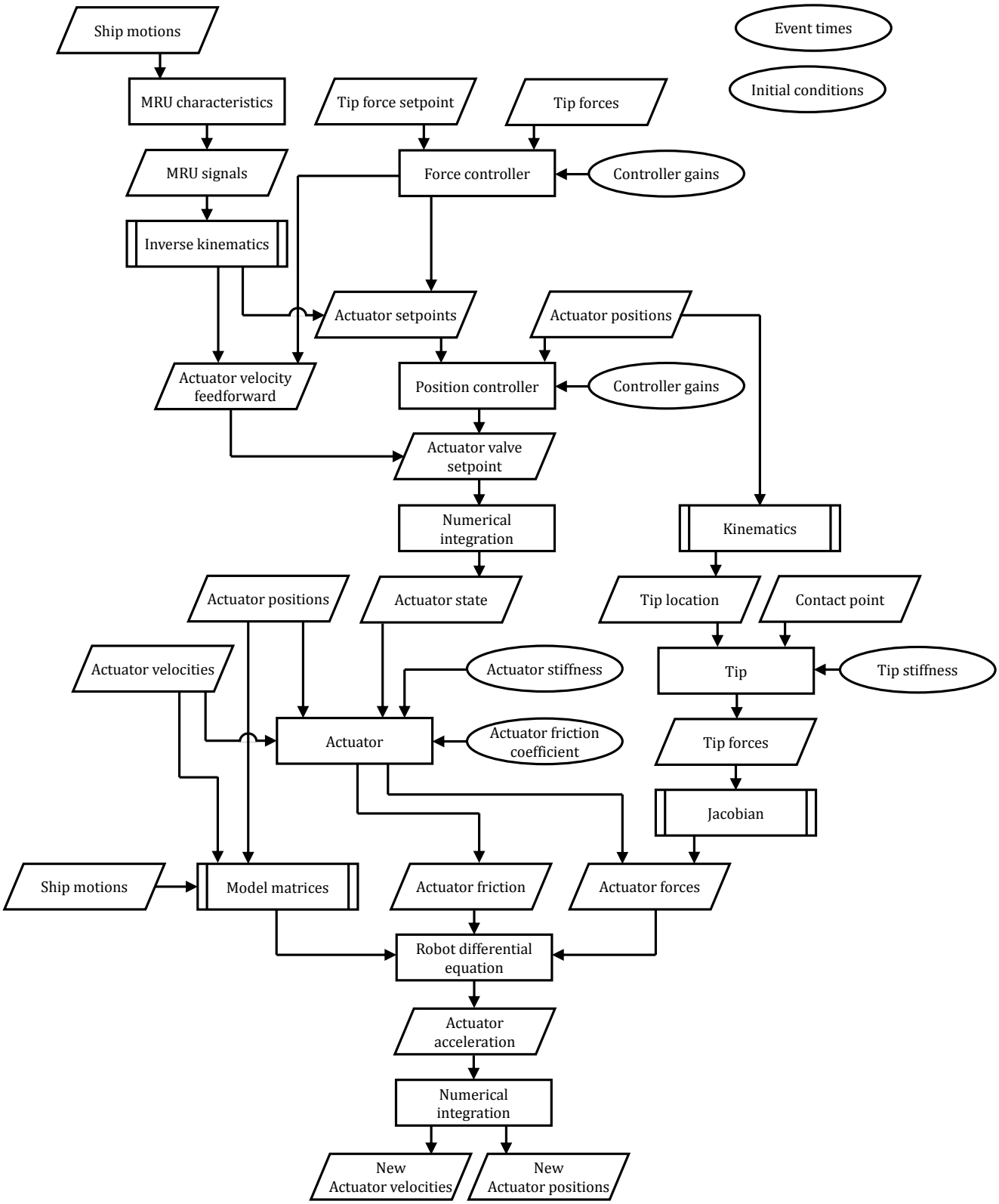

Figure 3-20: Flowchart of 3D model functions and variables.

Chapter 4

Force Control

4-1 Tip Forces

The mass of the actuator is fixed to the environment through a flexible tip with stiffness K_{tip}. Up to this point all modeling has been done in 3D and kinematic relations were needed to translate a tip position to actuator angles and vice versa. For the synthesis and analysis of the force controller only the telescope actuator is considered with the gangway in horizontal position. Therefore no kinematics are required and the problem becomes one dimensional. The simplified one dimensional model is shown in Figure 4-1 without and with the tip fixed.

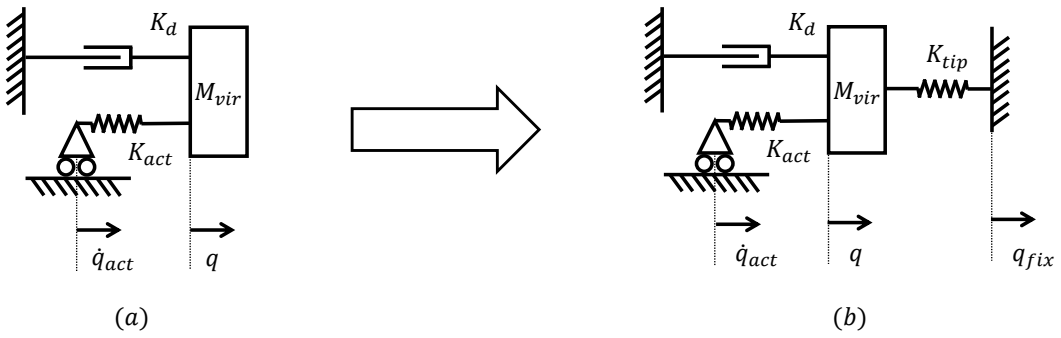

Figure 4-1: (a) Hydraulic actuator with mass in position control. (b) Same actuator but connected to environment through flexible tip with stiffness K_{tip}.

Here, M_{vir} is the mass of the moving part of the gangway, referred to as the second telescope (T2). K_{act} and K_d are the combined stiffness and friction of the hydraulic motor and the cables that connect the second telescope. K_{tip} is the stiffness of the rubber tip on T2 which is in contact with the offshore structure. Notice that the system is seen from the ship reference frame, and thus ship movement results in the movement of the environment (q_{fix}). With the tip connected to the environment, Figure 3-1 is extended with the environment movement

and a natural feedback of the tip force on the load. The block diagram is shown in Figure 4-2. This is the position controlled system without force control.

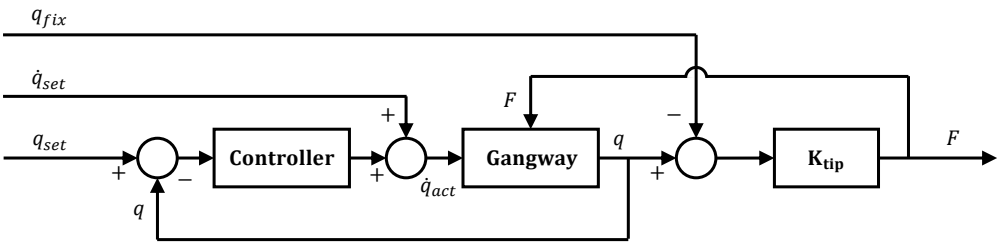

Figure 4-2: Block diagram for gangway in position control with tip fixed. Without force control.

Important characteristics of the system that are relevant to the syntheses of the force controller are summarized as follows.

1. The hydraulic valve will act as an ideal velocity source.
2. The movement of the environment is forced and can be seen as a disturbance.
3. The force on the environment is relevant and differs from the force in the actuator.
4. Force tracking on the moving environment is required instead of impedance control.
5. Complexity of control structure is limited due to implementation in Programmable Logic Controller (PLC) computers.

4-2 1D problem analysis

The block diagram shown in Figure 4-2 can be written in detail using the position controller and the gangway dynamics from Figure 3-6. The detailed dynamics are shown in Figure 4-3. Here $\dot{q}_{set}$ is the actuator velocity setpoint calculated from using the Motion Reference Unit (MRU) signals and $\dot{q}_{fix}$ is the actual movement of the environment.

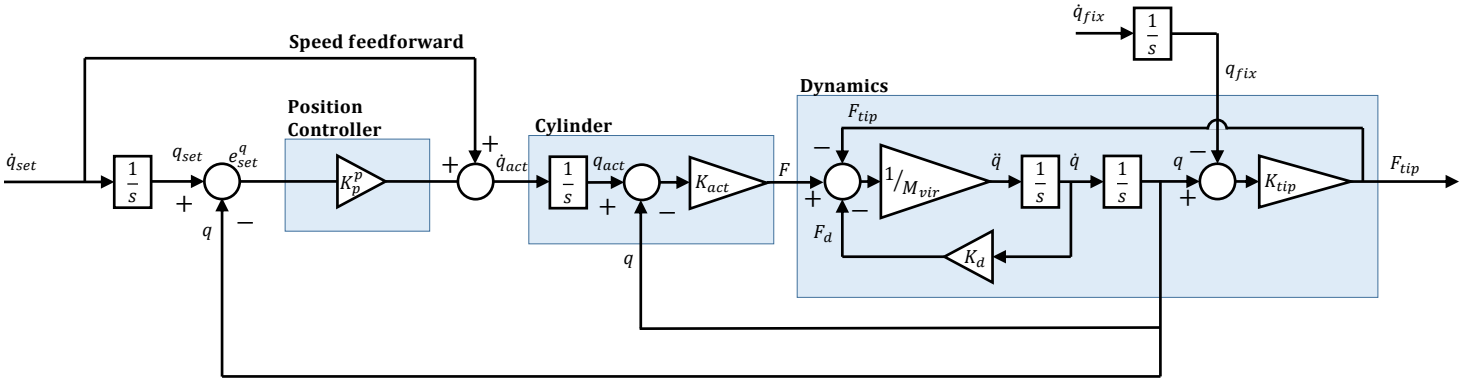

Figure 4-3: Flowchart of 3D model functions and variables.

The transfer functions from the actuator setpoint and the environment movement can be extracted for sensitivity analysis. The equation for the total system is shown in (4-1).

$$F_{tip} = P(s)\dot{q}_{set} + P_d(s)\dot{q}_{fix} \tag{4-1}$$

In case of perfect MRU behaviour, $\dot{q}_{set}$ will be the same as $\dot{q}_{fix}$ and (4-1) is simplified, shown in (4-2).

$$F_{tip} = \big(P(s) + P_d(s)\big)\dot{q}_{fix} \tag{4-2}$$

Bode plots for these transfer functions are shown in Figure 4-4. The block diagram in Figure 4-3 reduces to the diagram shown in Figure 4-5. Notice that $P(s)$ shares multiple states and parameters with $P_d(s)$, therefore $P(s)+P_d(s)$ can result in a system with higher orders, these can be reduced by pole zero cancellation.

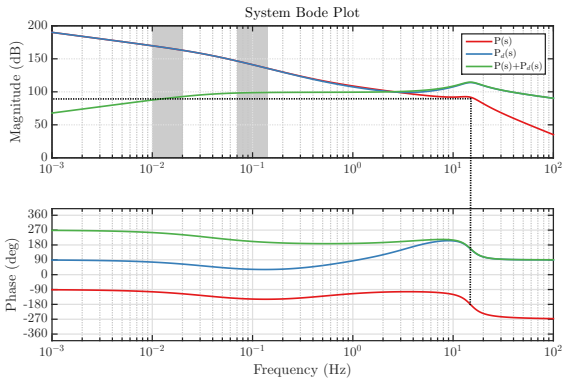

Figure 4-4: Transfer functions from velocity setpoint, fixed tip velocity and controlled fixed tip velocity to tip forces.

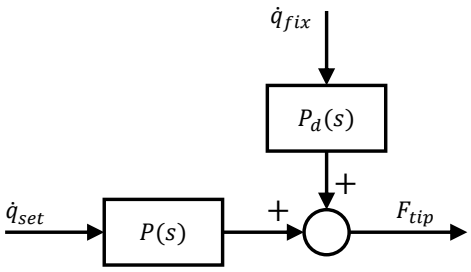

Figure 4-5: Simple representation of position controlled system with tip landed.

The 180 degree phase difference between $P(s)$ and $P_d(s)$ results in a large reduction of tip forces in the low frequency region when MRU signals are perfect. This is not the case in reality, especially for these low frequency movements. In Section 3-3 has been shown that the higher frequency movements can be cancelled to up to 95%. The simplified representation in Figure 4-5 can be extended by a negative feedback force controller $K^f(s)$ as shown in Figure 4-6.

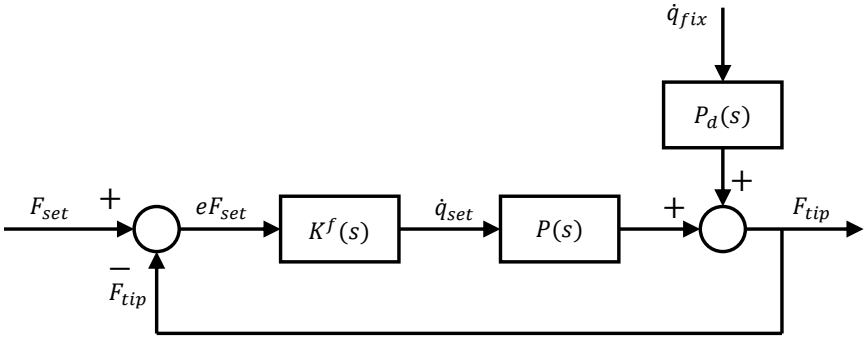

Figure 4-6: Position controlled system with force feedback and arbitrary force controller.

The control output will be used directly as a speed feedforward setpoint to the actuators in $P(s)$. The equation for the tip force as a function of the force setpoint and the external movement is shown in (4-3).

$$F_{tip} = \underbrace{\frac{P(s)K^f(s)}{1+P(s)K^f(s)}}_{T(s)} F_{set} + \underbrace{\frac{1}{1+P(s)K^f(s)}}_{S(s)} P_d(s)\,\dot{q}_{fix} \tag{4-3}$$

In this representation the loop transfer, sensitivity, and complementary sensitivity can be respectively defined as:

$$\text{Loop transfer} \qquad L(s) = P(s)K^f(s) \tag{4-4}$$

$$\text{Sensitivity} \qquad S(s) = \frac{1}{1+P(s)K^f(s)} \tag{4-5}$$

$$\text{Complementary sensitivity} \qquad T(s) = \frac{P(s)K^f(s)}{1+P(s)K^f(s)} \tag{4-6}$$

The sensitivity is a useful metric to determine the how the system rejects disturbances. In this case the disturbance is the fixed tip movement. Which is multiplied with the disturbance dynamics $P_d(s)$ before it enters the loop. The complementary sensitivity quantifies how the system will track the force setpoint. The open loop transfer will be used to determine the stability of the system by closing the loop and mapping the pole locations using the root locus method.

4-3 Controller design

4-3-1 Proportional force control

The proposed proportional force control is a controller which measures the tip force and uses this in a negative feedback loop. The tip force error is multiplied with the controller gain, the

resulting signal is fed directly to the actuator as a speed setpoint. A higher tip force error results in a higher actuator speed, thus reducing the tip forces. The actuator speed setpoint is integrated and added to the neutral position which is used in position control.

The bode plot for the plant $P(s)$ can be used to determine the gain and phase margins of the controlled system, see Figure 4-4. Here, the gain margin is -91.8 dB, the phase approaches -270 degrees where the magnitude crosses the 0 dB line. Which results in a negative phase margin of -89.1 deg and thus, the system will be unstable for a unit feedback gain. The gain margin of -91.8 dB indicates that the system will be stable with a gain of $2.57 * 10^{-05}$ or lower. This small gain is expected since the tip force is used to apply a speed setpoint. Due to the high tip stiffness small displacements can lead to high forces. Closing the loop with a variable feedback gain gives the root locus plot shown in Figure 4-7. Figure 4-8 zooms in to show the details at the origin.

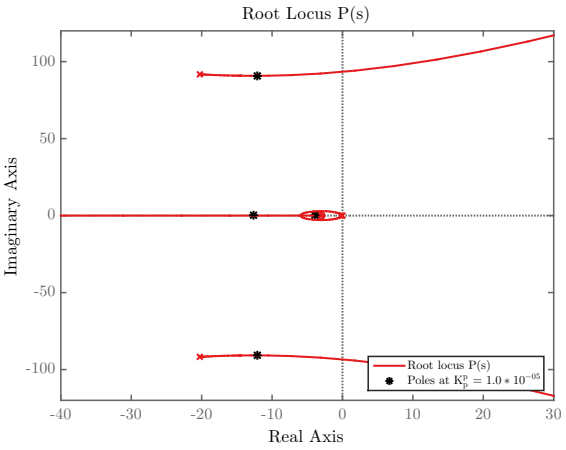

Figure 4-7: Root locus for the proportionally controlled system.

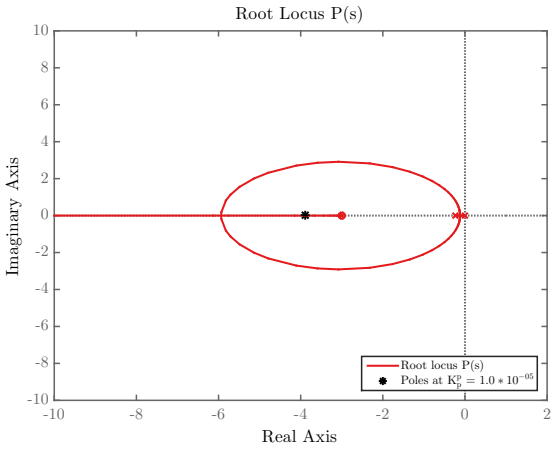

Figure 4-8: Detail of root locus for the proportionally controlled system.

The root locus crosses the vertical axis into the right half plane at a gain of approximately $K_p^f = 2.57 * 10^{-05}$. The black asterisks indicate a proportional gain of $K_p^f = 1 * 10^{-05}$. For this gain the majority of the poles share the same vertical axis. There is however a zero in the open loop transfer function. This zero has a value of -3 and is close to the imaginary axis. The zero is a result of the proportional position controller, which has a gain of $K_p^p = 3$. Therefore, the contribution of the proportional controller might be slow.

Next, the sensitivity is shown for a selection of proportional gains. The sensitivity multiplied with the disturbance dynamics $P_d(s)$ gives the response from the ship velocity to the tip force. This relation might be non-intuitive since the ship motions are defined in positions instead of velocities. Therefore, the derivative $s(S(s) * P_d(s))$ is shown.

Two regions are highlighted in the magnitude plot, one area from 0.01 to 0.02 Hz and one from 0.07 to 0.14 Hz. These regions present the low frequency and the high frequency contributions which are present in the ship movements. The low frequency movements may go unobserved by the MRU which applies high pass filters to eliminate drift. The higher frequency movements will be reduced up to 95% by position control. These frequencies correspond to motions with

a period of approximately 60 seconds for the low frequencies and a period of approximately 10 seconds for the high frequencies, as shown in Section 2-3, Figure 2-6.

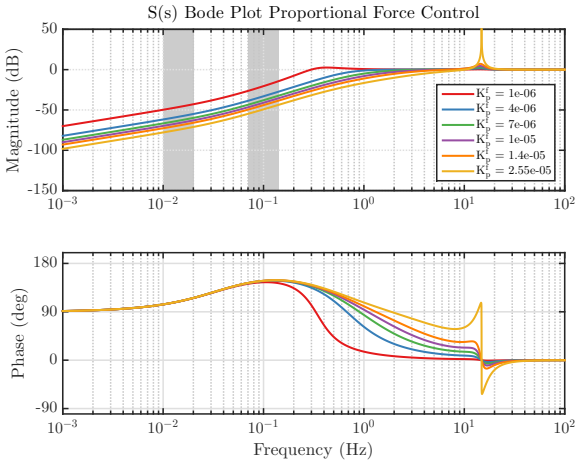

Figure 4-9: Sensitivity of the system with proportional control.

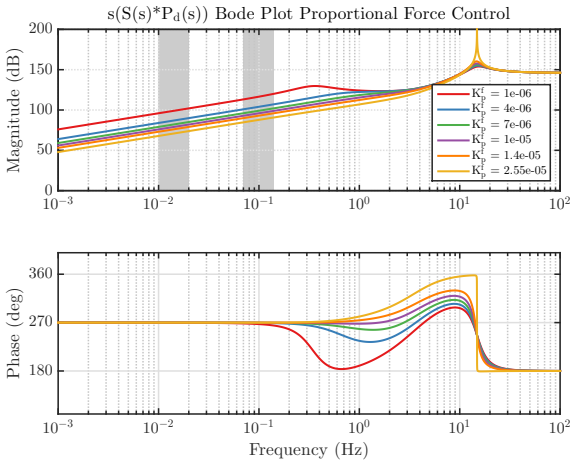

Figure 4-10: Sensitivity multiplied with the disturbance dynamics under proportional control.

Figure 4-9 shows the effect of Bode's sensitivity integral, also known as the waterbed effect. Higher feedback gains lead to more reduction in the low frequency area, but with a cost. A resonance peak appears at approximately 14 Hz. With a gain of $K_p^f = 1*10^{-05}$ this resonance peak reaches 4.5 dB or a magnitude of 1.68. This can be a problem when the gain is increased.

Figure 4-10 shows the transfer function from the fixed position to the tip force. It can be clearly seen that with increasing gains a limit is approached to the performance of the proportional force controller. The gain of $K_p^f = 2.55*10^{-05}$ is only just stable, but in practice this controller will not be feasible. The earlier determined controller gain of $K_p^f = 1*10^{-05}$ displays a gain of 82 dB in the low frequency area and a gain of 98 dB in the high frequency area. For an amplitude of 1 meter, this correspondents with forces of 1100 Kg in the low frequency range and forces of 400 Kg in the high frequency area for a residual motion of 5 cm. Assuming 95% of the motions are cancelled by the position controller. These force variations will not meet the objective defined in Section 2-4.

4-3-2 Derivative and Proportional-Derivative force control

In Figure 4-4 can be seen that the open loop has a negative phase margin of -89.1 deg which results in an unstable system when the loop is closed. A stable system can be obtained by decreasing the feedback gain, or by adding phase. A low feedback gain has been applied in Section 4-3-1, in this chapter we will investigate the effect of adding phase to the system.

Derivative control adds a 90 degree phase shift which can be used to achieve a stable closed loop system. Derivative control has the disadvantage that it attenuates high frequency signals, see Figure 4-11. The high frequency noise in the measured tip force signal will be amplified which has consequences for the performance of the system. A pure derivative controller as well

as a proportional-derivative controller are examined. Figure 4-12 shows the loop transfers for the uncontrolled system, the pure derivative control, and the proportional-derivative control.

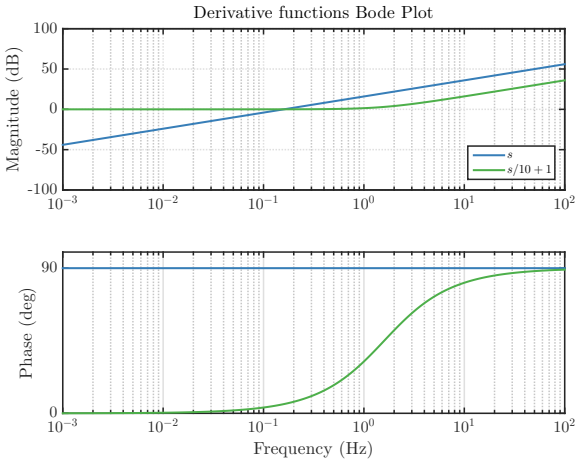

Figure 4-11: Bode plots of D and PD controllers applied in the system.

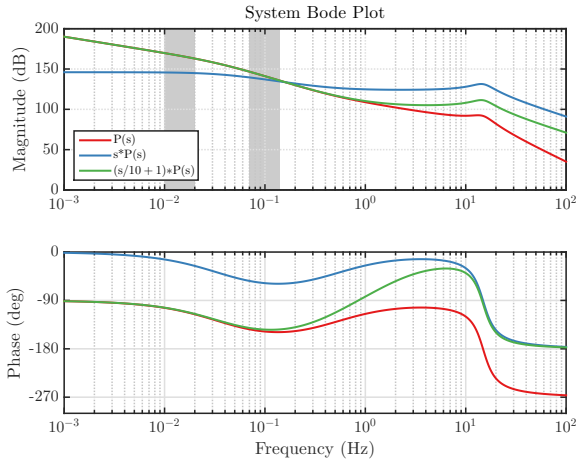

Figure 4-12: Loop transfer of system dynamics with derivative controllers.

The loop transfers of the derivative controlled systems shown in Figure 4-12 both have an infinite gain margin, but their phases approach -180 very closely at the point where the plot crosses the 0 dB line, this is problematic for robustness of the system. From the sensitivity plot for the pure derivative controller shown in Figure 4-13 it can be seen that increasing the gain keeps decreasing the magnitude of the response for low frequencies. However, the waterbed effect has a large effect on the resonance peak at high frequencies. The same effect is observed in the transfer function from the ship movements to the tip forces. Nevertheless, the disturbances in the low and high frequency ship movements are well rejected.

For a derivative gain of $K_d^f = 0.0004$, the magnitude in the relevant frequency ranges is 68 dB, which corresponds with a variation of approximately 250 kg for amplitudes of 1 meter. Increasing the gain to $K_d^f = 0.001$ reduces the force variations further to approximately 100 kg. Unfortunately, the addition of noise, the low phase margin, and the resonance peaks makes this solution unsuitable for application in practice.

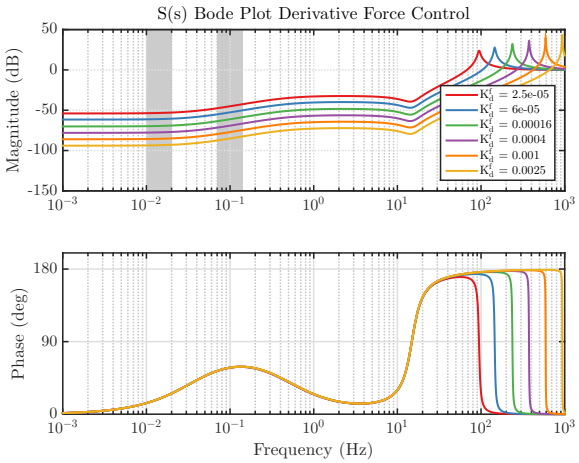

Figure 4-13: Sensitivity of the system with pure derivative control.

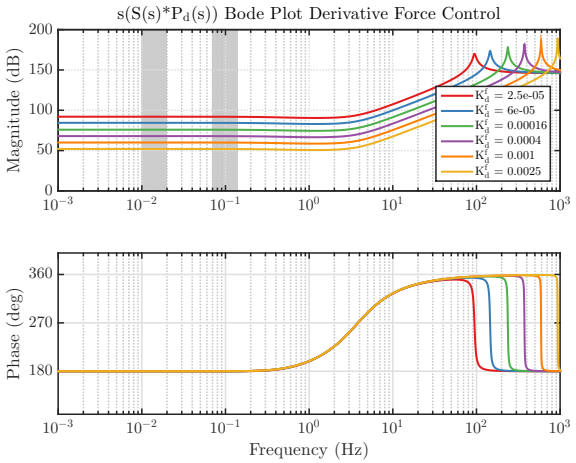

Figure 4-14: Sensitivity multiplied with the disturbance dynamics under pure derivative control.

For the proportional-derivative controller the location of the zero was placed at -10 as such that the 90 degree phase is added at the critical point. For the lower frequencies the magnitude of the response is the same as the controller gain, see Figure 4-11. The cut off shows to be effective in decreasing the disturbance in the lower frequency regions with respect to the pure derivative controller. The controller with gain $K_d^f = 0.0004$ was able to reduce the low frequency force variations even further to 30 Kg, see Figure 4-16. The high frequency resonance peaks are also present. The system is expected to be fast, but small changes in dynamics or noise can make the system unstable. Therefore, derivative controllers are not suitable for this application.

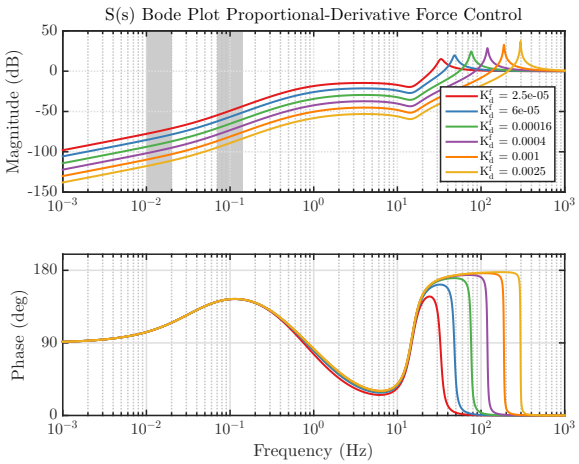

Figure 4-15: Sensitivity of the system with proportional-derivative control.

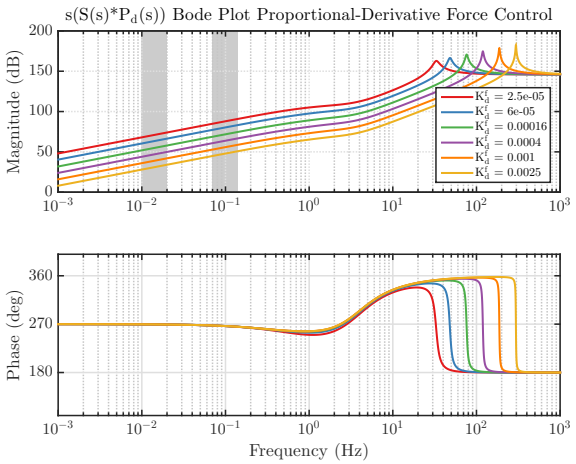

Figure 4-16: Sensitivity multiplied with the disturbance dynamics under proportional-derivative control.

4-3-3 Proportional-Integral force control

Hydraulic actuation can be characterized by an ideal velocity source. This has been discussed in Section 3-1. The valves that control the oil flow to the actuators have a high bandwidth, combined with an excess of hydraulic pressure and flow capacity, the desired flow will be realized when needed.

The hydraulic flow drives a mass with inertia, the oil in the actuator will be compressed and acts as a spring delivering a force to the mass. Driving an ideal velocity source is physically not possible, however, the acceleration of the hydraulic fluid can be neglected. And thus, the ideal velocity source can be represented by a mass-less cart. See Figure 4-1. The actuator thus works as a single integrator, with a velocity input and a position output. This position is linearly related to the force on the mass system through oil compression. This explains why the root locus for proportional force feedback showed a lot of resemblance with a bode plot for integral feedback, see Figure 4-7.

One solution to control the force on the mass is by cancelling the valve dynamics. However, one derivation already amplified the high frequency noise, a PDD-controller would not be realistic. Other solutions exist by using direct feedforward techniques to cancel the natural feedback in the force on the mass. This has been described in literature [20].

We are not looking in controlling the internal force on the mass but the force on the environment. The actuator position can be controlled instead. In order to do so lets review a conventional PID-controller shown in the top image in Figure 4-17. Here, a force is measured and fed in to the PID-controller, this force is linearly dependent on the mass position x through a spring constant k. The output of the controller is a force exerted on the mass which results in an acceleration $\ddot{x}$. After two integrators, the new position is obtained.

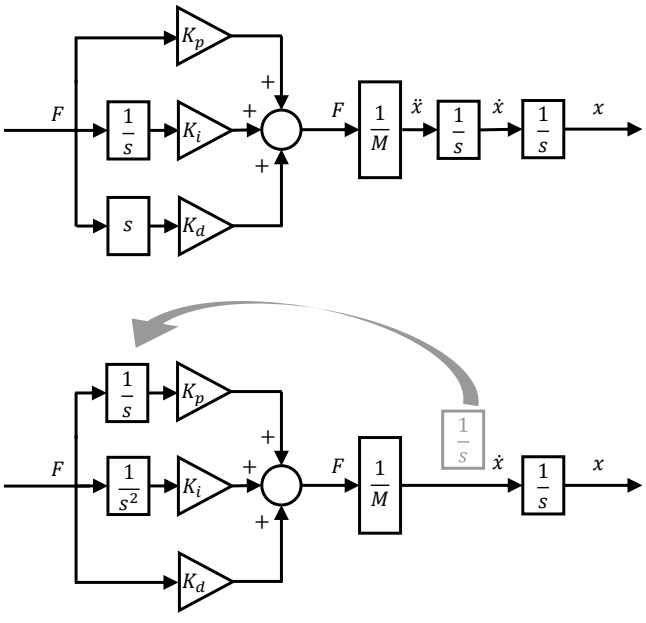

Figure 4-17: Using a PID controller to regulate speed.

Dealing with an hydraulic actuator cuts out the first integrator. The output of the controller

is a valve setpoint, directly related to a hydraulic flow. If the same PID-controller is applied, each component will start giving different responses from the force input to the position x. To restore the expected behaviour of each component, the integrator should be added to the controller, as shown in Figure 4-17. Now, the PID controller has become a PII controller. However, since one integrator is removed, the integrator will behave like the proportional controller and the proportional controller will behave as the derivative controller. As if applied to a normal second order system. Therefore it is useful to study the effect of a PI controller for tip force control.

The previously mentioned effects will be demonstrated in a root locus plot of the loop transfer with PI-force control. A PI controller with a zero at -30 and a gain of $1.253 * 10^{-05}$ is applied. The controller is rewritten such that the contribution of individual components can be changed:

$$K_f(s) = 1.253 * 10^{-05} \left(\frac{s + 30}{s} \right) \tag{4-7}$$

$$= 1.253 * 10^{-05} + 1.253 * 10^{-05} \left(\frac{30}{s} \right) \tag{4-8}$$

Two root loci are plotted in Figure 4-18. In the first root locus plot, the integral contribution is varied and the pole trajectories shown. The second root locus plot varies the proportional contribution. The integral poles follow a vertical trajectory which is characteristic for proportional control and the proportional poles circle around the origin, which is normal for derivative control. Only two out of the four poles display these characteristics, these are the poles related to the actuator position.

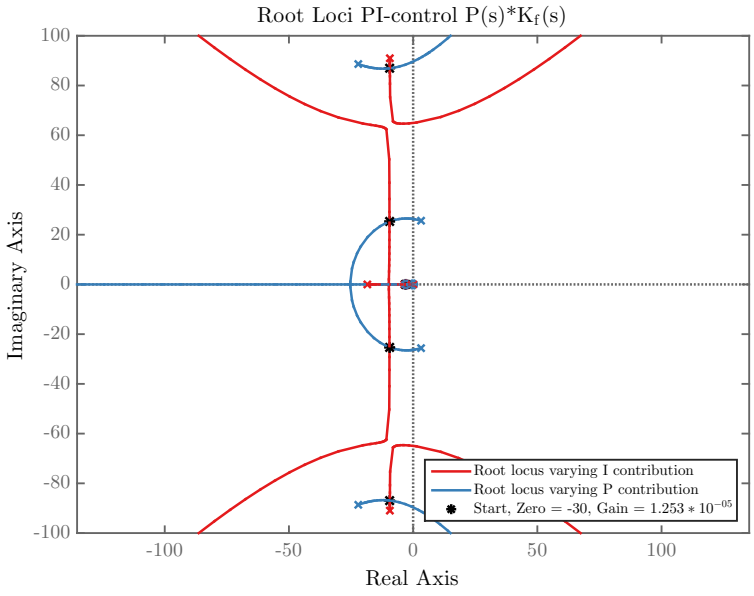

Figure 4-18: Root locus pole trajectories for individual P and I variations.

The location of the zero in the PI-controller determines the cut off frequency, or also defined as time constant. For a time constant of 5 seconds or 0.2 Hz, the pole location will be

$-2\pi/5 = -1.257$. Figure 4-19 shows the bode plots of three feasible PI-controllers. Two controllers with a time constant of 15 and 5 seconds. And one controller with a zero at -30, which corresponds with a time constant of 0.209 seconds. The low proportional gain at higher frequencies bring stability to the system, see Figure 4-20.

The PI-controller with the zero at -30 is expected to better dampen the motions in the low frequency regions, but at the cost of the phase margin, which is reduced from 71 to 27 degrees with respect to the PI controller with the 5 second time constant. Observe that there is a positive gain margin indicated with a line. There is however a negative gain margin present as well. The proportional position controller adds a zero at -3, this causes the dip in phase around 0.1 Hz which pulls the phase below 180 degrees. This will not cause any further problems.

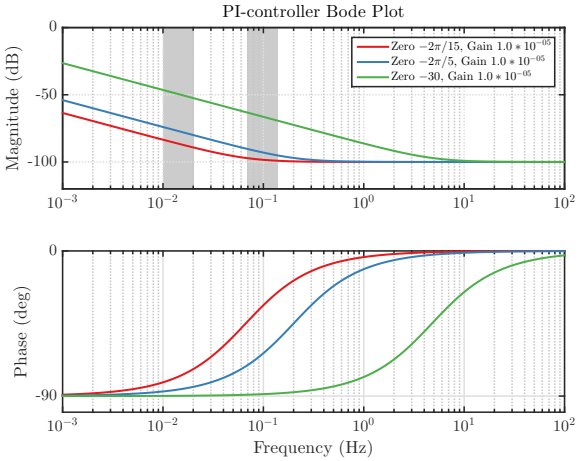

Figure 4-19: Bode plots of PI controllers applied in the system.

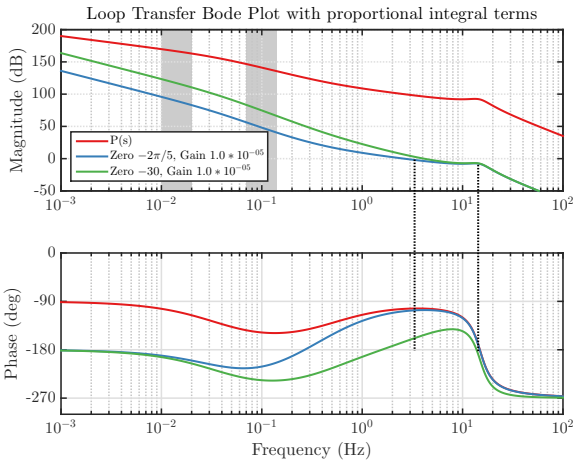

Figure 4-20: Loop transfers of system dynamics with proportional integral controllers.

Figure Figure 4-21 and Figure 4-22 show the root locus plots for different zero locations. Every controller suffers from the instability at low gains.

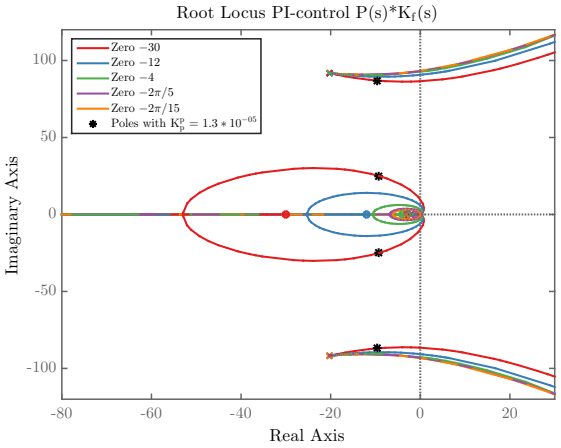

Figure 4-21: Root locus of PI-controlled system with varying zero locations.

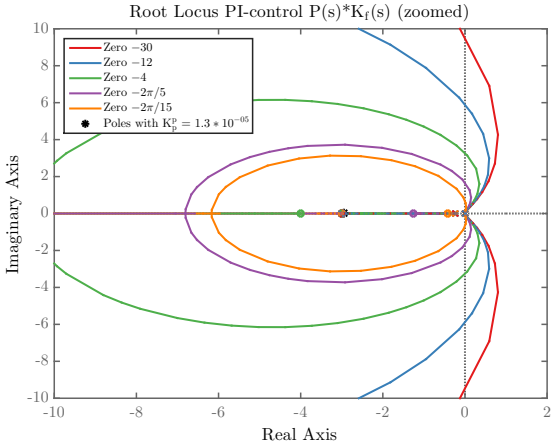

Figure 4-22: Detail of root locus of PI-controlled system with varying zero locations.

First, the PI-controller with the zero at $-2\pi/5$ has been implemented. The sensitivity is shown in Figure 4-23. A significant reduction is seen in the low frequency range. The low gain controller does show a low frequency resonance peak. This is not a problem for the higher gain controllers. Figure 4-24 shows the power density from the external movements to the tip forces. The regions of interest are highlighted, the low frequency range can go unnoticed by the MRU sensors and in the high frequency range, residual motions of 5% are expected. In the low frequency range, a magnitude of 54 dB is present. Which corresponds with approximately 50 Kg. The higher frequency range has an amplification of 87 dB. Which results in forces of approximately 110 Kg due to residual motions of the position control system.

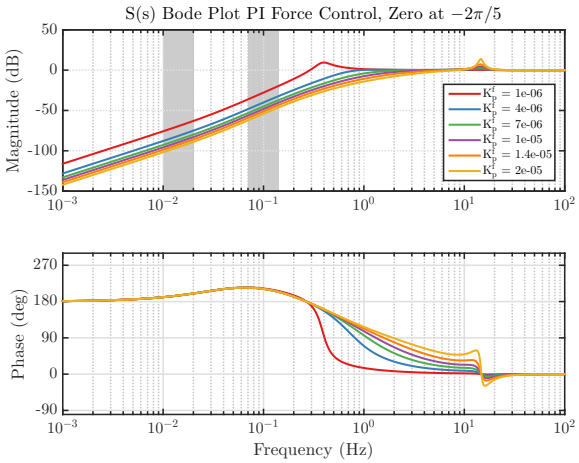

Figure 4-23: Sensitivity of the system with proportional-integral control with zero location at -2pi/5.

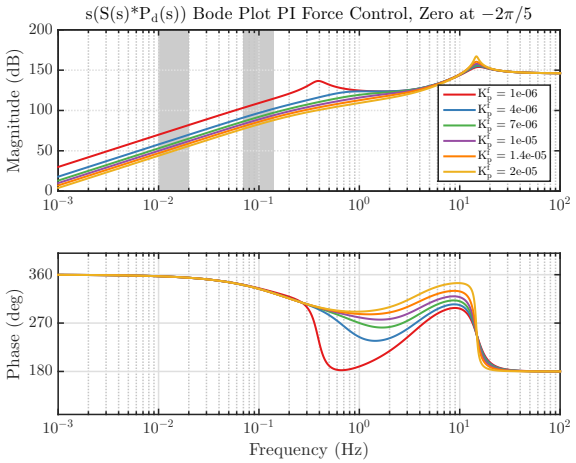

Figure 4-24: Sensitivity multiplied with the disturbance dynamics under proportional-integral control with zero location at -2pi/5.

The sensitivity plot for the PI controller with the zero at -30 is shown in Figure 4-25. A

higher decrease is present for the low frequencies which results in more amplification in the higher frequency ranges due to the waterbed effect. The low gain controller has become unstable. Whereas the controller with the gain $2 * 10^{-05}$ performed good for the higher time constant controller, it might introduce oscillations in the higher frequency areas.

The controller with gain $1.4 * 10^{-05}$ looks like a better option with a resonance peak at 8.5 dB instead of 20 dB. The power density of the PI controller with the zero at -30 shows promising results, see Figure 4-26. The controller with a gain of $1.4 * 10^{-05}$ has an amplification of only 32 dB at the low frequency range, which corresponds with only 5 Kg variation for 1 m movements. The higher frequency region is amplified with 64 dB, combined with the 95% reduction of motions due to the position controller. This results in a force variation of 8 Kg for 1 m movements. These results should be possible in theory, however, in practice this might not be the case.

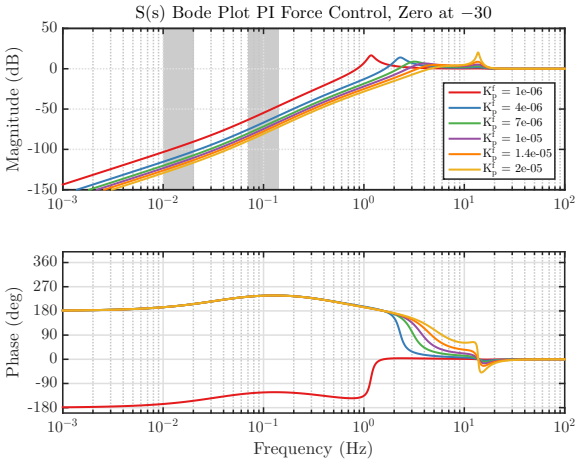

Figure 4-25: Sensitivity of the system with proportional-integral control with zero location at -30.

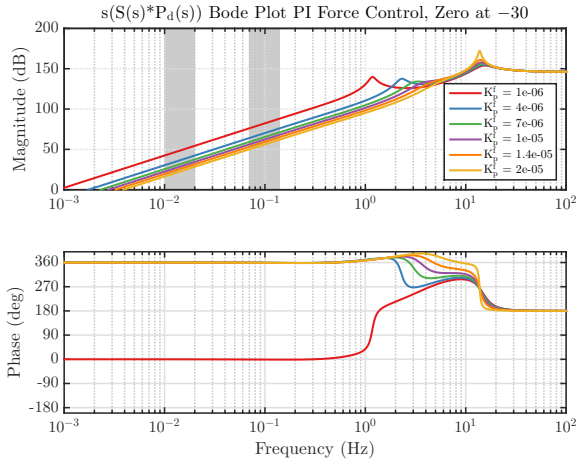

Figure 4-26: Sensitivity multiplied with the disturbance dynamics under proportional-integral control with zero location at -30.

4-3-4 Comparison of Force controllers

Figure 4-27 shows a collection of the controllers that have been considered. P-control does the job and is stable, but lacks performance overall. When a derivative term is introduced, enough suppression of the lower frequency disturbances is possible, but introduces large oscillations in the high frequency area. PI-controllers are proven to be very efficient in rejecting the low frequency movements. For example the PI-controller with a zero at $-2\pi/5$ performs well for low frequency movements, but can be improved for the higher frequencies. Disturbance rejection is improved by increasing the gain, this will also increase the oscillation peak at higher frequencies. A higher reduction can be given by shifting the zero to the left. For example the PI-controller with the zero at -30.The loss in phase margin can be solved by reducing the gain. Which leads to a controller with a better reduction in the low frequency region and a lower peak at the high frequencies.

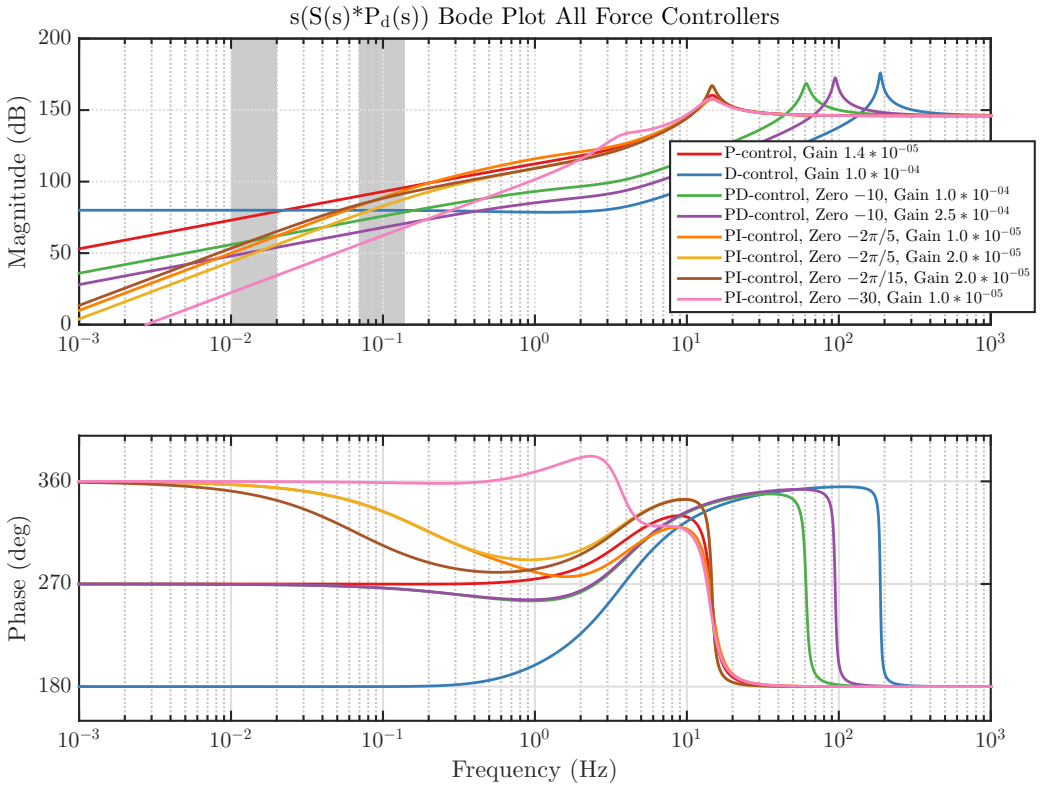

Figure 4-27: Complete overview of all control structures considered during design.

4-3-5 Force controllers in 3D model

The three best performing PI-force controllers have shown to perform in the frequency domain. The force variations estimated from the power spectral density (PSD) plots are shown in Table 4-1. The force controllers have been applied in the 3D model over a period of 5 minutes.

Table 4-1: Expected force variations for designed PI controllers.

Controller	Magnitude [dB]	Force variations [Kg]
PI-control, Zero $-2\pi/15$, Gain $2.0 * 10^{-05}$	90	160
PI-control, Zero $-2\pi/5$, Gain $2.0 * 10^{-05}$	86	100
PI-control, Zero -30, Gain $1.0 * 10^{-05}$	66	5

The results are shown in Figure 4-28. The controllers perform better in the simulations then expected. In the frequency domain a reduction of 95% was assumed, however, from the 3D model results it is shown that the gangway performed a bit better than the estimated 95%. This might be the reason why the force variations are lower than expected. However, the order of magnitude is correct and all the controllers perform equally better as predicted.

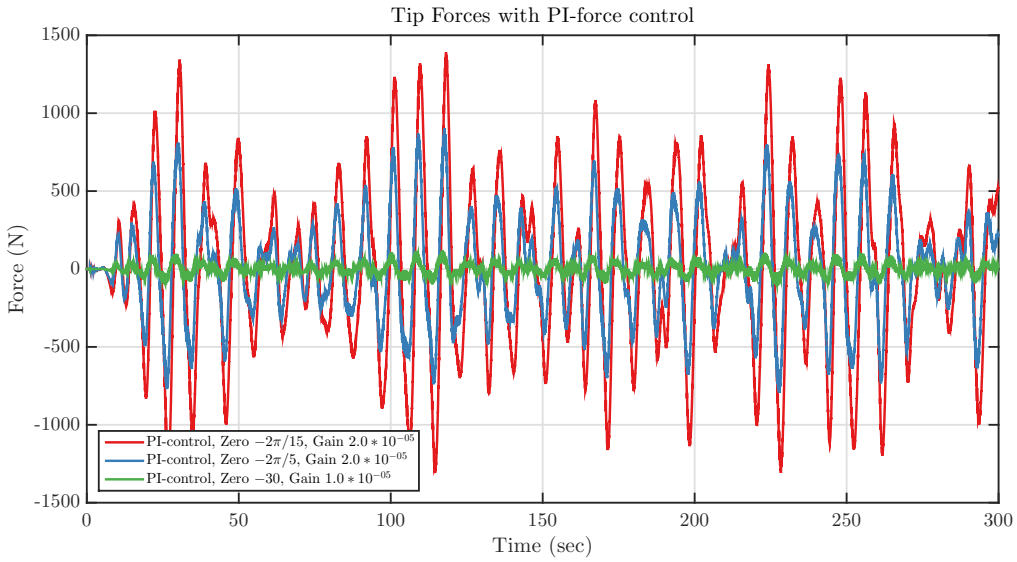

Figure 4-28: Result of force controllers tested using the 3D model in time domain.

Chapter 5

Results

5-1 Offshore testing

Sea trials have been conducted at offshore wind farm Luchterduinen in the North Sea. Due to safety restrictions, the first landings have not been performed on the transition piece but directly on the structure of the monopile, see Figure 5-1. A GoPro camera was mounted facing the tip, this allowed for close analysis of the tip compression, see Figure 5-2.

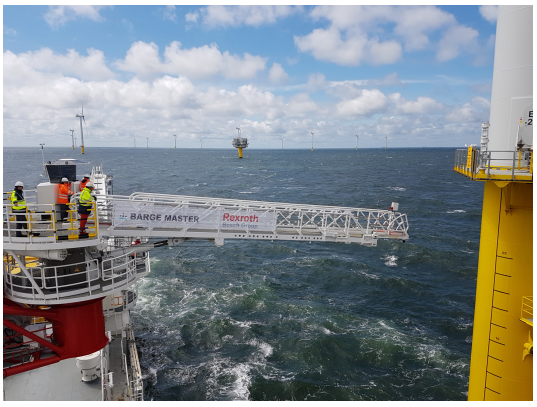

Figure 5-1: Test location at wind farm Luchterduinen.

Figure 5-2: GoPro footage from landed tip with tip compression visible.

During sea trials, the first tests have been performed with a pure proportional force feedback controller as shown in the control diagram shown in Figure 4-6 with a proportional gain of $2.5 * 10^{-5}\ m/s^2/N$. Figure 5-3 shows the tip force in x-direction with a setpoint of 400 kg. The response is stable, however, the performance is very bad. An oscillation of 1000 kg is observed. The tip force oscillates until a negative tracking error of more than -400 kg occurs which causes the tip to lose contact. After that, the gangway attempts to regain contact and a collision occurs.

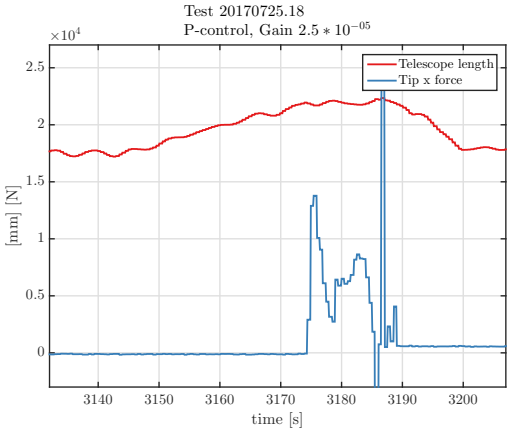

Figure 5-3: Tip force with low gain proportional force control.

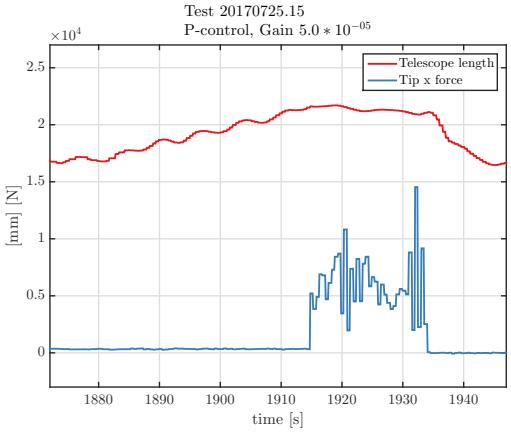

Figure 5-4: Tip force with high gain proportional force control.

The controller in Figure 5-3 did not show any unstable behaviour, therefore an attempt was made with an increased proportional gain. The gain was increased to $5.0 * 10^{-5}\ m/s^2/N$. The same setpoint of 400 kg was applied. The result is shown in Figure 5-4. Now, an unstable situation is created. This situation matches with the root locus plot seen in Figure 4-7. As predicted, the performance will not reach acceptable levels with pure proportional control. Implementation of the proposed PI-controller yielded better results. As shown in Figure 5-5. The proportional gain was decreased to $2.0 * 10^{-5}\ m/s^2/N$ with an integrator time constant of 15 seconds. Oscillations are higher than the predicted 160 Kg, and of unacceptable levels. But contact is maintained.

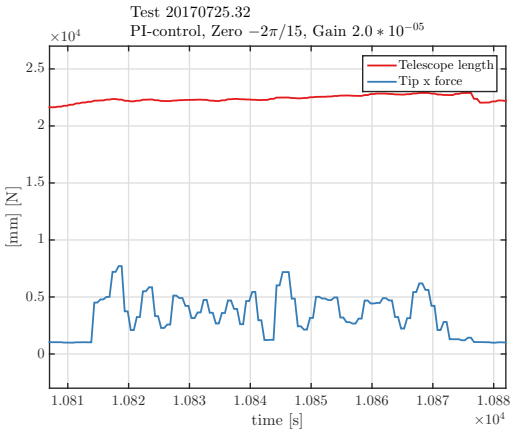

Figure 5-5: Tip force with high time constant proportional-integral force control.

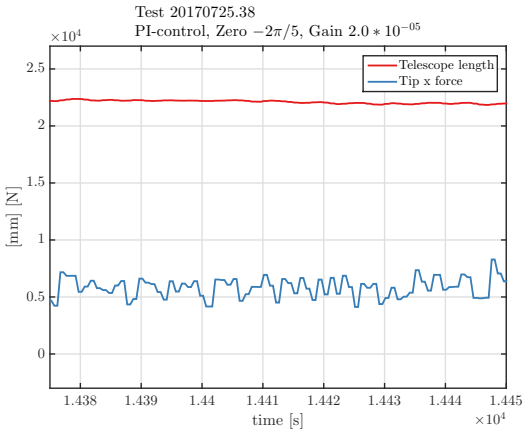

Figure 5-6: Tip force with low time constant proportional-integral force control.

After tuning, the best performing PI-controller values were $2.0 * 10^{-5}\ m/s^2/N$ with an integrator time constant of 5 seconds. The setpoint was increased to 600 kg. The result is shown in Figure 5-6. Again, the force variations are higher than predicted. An average variation of 120 Kg is achieved. Which matches the predicted value of 100 Kg quite close. In reality there are always unmodeled factors which play a significant role. Simulations showed that

lower time constants should yield a better performance. But in reality lower time constants started showing unstable responses, this might be due the phase loss that was predicted in Section 4-3-3.

Chapter 6

Conclusion and recommendations

The offshore industry is constantly exploring new solutions to further improve the process of safely transferring personnel and cargo from moving ships to offshore structures. The Barge Master Gangway provides a solution to establish a safe connection between a moving ship and a static offshore structure. The work of this thesis work can be grouped in two subjects. First a 3D model was created in which all the sensors, actuators and environmental influences were modeled. This 3D model was used to simulate general scenarios and validate assumptions which have been made during the conceptual design. The second part of this thesis deals with the design of a control structure in which hydraulic actuators are used to track a force setpoint on a surface with imposed movement. This problem of hybrid position and force control was solved by isolating a one dimensional time invariant linear model. This model was used to understand the dynamics of the set-up and the design of a simple controller. A simple controller structure was required for practical implementation in the Programmable Logic Controller (PLC)s. Stability and performance of the force controller have been analyzed using this model. Finally, the control structure has been implemented in the software of the gangway during sea trials. Tests have been performed before and after implementation which showed a significant improvement. The results of these tests have been compared to the results from the simulations. The conclusions from these three parts have been described in the following sections.

6-1 3D model

The 3D model was used to verify the operational range of the actuators for speed, force, and power. Kinematic relationships and inverse kinematics have been tested in the model and later implemented in the software. MRU drift has been applied on the model which showed that the force controller was able to cope with these uncertainties. The effect of the non-inertial frame of reference resulted in an improved performance for the same relative actuator setpoints. This allowed for conservative simplifications in the linear hydraulic model. The combination of simultaneous actuator movements to ship movements in six degrees of freedom

resulted in a clear performance value for absolute tip position error as well as a force error magnitude and direction. Controller structures in the Laplace domain have been converted to discrete time filters and tested in the discrete time 3D model. An attempt was made to model the deflections of the gangway. The results of the flexible dynamics during position control show reliable results. However, the process of validation was beyond the scope of this report. It is expected that the boundary conditions of the deflections in landed position are more complex than initially anticipated and thus will be left for future research.

6-2 Linear hydraulic model and force control

The force control problem consists of three factors that make this problem unique. First, hydraulic actuators work as ideal velocity sources. The second property is the forced movement of the environment. In other words, the actuator is constrained between the base and the environment. The third factor is non-collocation, the goal is to regulate the force on the environment as opposed to the force in the actuator. A fourth factor, the static tip on a moving base setup has been shown to result in a conservative estimate of performance when modeling in an inertial reference frame. For controller design, a linear time invariant model has been developed in one dimension. The environment velocity will be modeled as a disturbance, the measured velocity feed forward which is used in position control can be isolated from the control diagram. The application of a typical ship movement power spectrum shows a disturbance rejection of 95 percent by the velocity feed forward. Furthermore, it is shown that there are no low frequency zeros in the open loop transfer function from the actuator input to the tip force, as opposed to the transfer from the actuator input to the actuator force due to natural velocity feedback. Therefore the positive actuator velocity feedback, which is popular in literature [21, 22], is not required. It is shown that due to the fact that a hydraulic actuator acts as an ideal velocity source, integral action is required in the feedback loop. The controller gain and the location of the zero in the PI-controller is determined using bode plots, the results are simulated in the time domain.

6-3 Test results

Testing can be divided in two phases, one test phase on land where a motion signal was simulated to generate a virtual setpoint on the actuators. The second test phase has been conducted during sea trials in its intended environment on the ship Vos Start operated by Vroon Offshore Services. The intention was to validate and identify all the parameters of the 3D model on land, however the amount of time for these tests was limited and the data collected was not useful for system identification. Separate parameters could be manually verified such as friction and masses but no hard conclusions could be drawn on the full dynamic range of the response. During sea trials, the proposed controller structure has been tested with and without the integrator. The expected response was observed in the proportional force controller. The proportional controller was unable to track the force setpoint and the tip disconnected, increasing the gains for the proportional controller resulted in an unstable system. Implementation of the PI-force controller resulted in a stable system with a performance within the acceptable boundaries.

6-4 Recommendations

As shown in Chapter 5, the performance of the force controller can be improved. Currently the force setpoint oscillates with an amplitude of approximately 150 kg. This is expected and can be reproduced in the simulations. The increase of the integral gain will lead to a lower time constant of the PI-controller. This will improve the performance. However, in practice, a higher integral gain leads to instability. This was not expected from the simulations. Further research should be done to identify this instability, whether it is a model parameter mismatch, or a factor which is unmodeled.

In [23], Seraji and Colbaugh propose an adaptive control scheme which shows promising results. It has not been considered in this thesis due to the PLC structure limitations. The adaptive force controller adapts the gains for different environments which could improve the performance.

This thesis has shown a start in deformation modeling using assumed modes, however, for this problem a more in depth analysis can be done on the flexibilities and their influence on the controller stability and performance. A re-evaluation can be done on the chosen method, as discussed by Schiavo et al. [24].

With enough confidence on the modeled dynamic flexibilities, an analysis can be performed for the friction forces in the plane of the environment in the same manner as performed in Chapter 4. However, the method might require some adaptations, for example, the mass cannot be considered as a point mass but will be distributed along the modeled spring.

Appendix A

Modern Robotics

A-1 Screw theory

Rigid bodies are represented by a collection of particles in a three dimensional coordinate frame. Rotation of a coordinate frame in relation to a different coordinate frame is represented by Euler angles in orthogonal 3x3 matrices. A rotation is composed of three rotations along the principal axis, x, y, and z. The orthonormal rotation matrices belong to the special orthogonal group $SO(n)$ this allows multiple rotations to be easily combined by multiplication as follows.

$$R_s^k = R_m^k R_s^m \tag{A-1}$$

A point in frame j can be represented by a vector in $\mathbb{R}^3$ and transformed to a point in frame i as follows.

$$p^i = R_j^i p^j \tag{A-2}$$

The three basis rotations are widely recognized and will be seen throughout this report.

$$R_x = \begin{bmatrix} 1 & 0 & 0 \\ 0 & \cos(\phi) & \sin(\phi) \\ 0 & -\sin(\phi) & \cos(\phi) \end{bmatrix}, \quad R_y = \begin{bmatrix} \cos(\phi) & 0 & -\sin(\phi) \\ 0 & 1 & 0 \\ \sin(\phi) & 0 & \cos(\phi) \end{bmatrix}, \quad R_z = \begin{bmatrix} \cos(\phi) & \sin(\phi) & 0 \\ -\sin(\phi) & \cos(\phi) & 0 \\ 0 & 0 & 1 \end{bmatrix}$$

A-1-1 Rotations and translations in 3D

The above formalism of rotations in 3D can easily be extended to rotations and translations in 3D. A point in frame i will be represented by a vector with three elements extended with a one.

$$P^i = \begin{bmatrix} p_x \\ p_y \\ p_z \\ 1 \end{bmatrix} \tag{A-3}$$

Then, rotations and translations are represented by a 4x4 transformation matrix in the form

$$H^i_j = \begin{bmatrix} R^i_j & p^i_j \\ 0^T_3 & 1 \end{bmatrix} \tag{A-4}$$

such that

$$P^i = H^i_j P^j \tag{A-5}$$

With $R^i_j \in SO(3)$ and $p^i_j \in \mathbb{R}^3$ these transformation matrices can also be combined by multiplication and thus:

$$H^k_s = H^k_m H^m_s \tag{A-6}$$

The inverse of a transformation matrix is the transformation in the opposite direction.

$$H^k_s = (H^s_k)^{-1} \tag{A-7}$$

A-1-2 Velocity of a rigid body: Twists

The velocity of a rigid body can be expressed using angular and translational motion. The velocity of a vector r which rotates around the origin with angular velocity ω is defined as the cross product of the two. In order to write this cross product as a matrix multiplication the skew-symmetric cross product matrix using tilde notation is introduced

$$\dot{r} = \omega \wedge r = \widetilde{\omega} r = \begin{bmatrix} 0 & -\omega_z & \omega_y \\ \omega_z & 0 & -\omega_x \\ -\omega_y & \omega_x & 0 \end{bmatrix} \begin{bmatrix} r_x \\ r_y \\ r_z \end{bmatrix} \tag{A-8}$$

For a point fixed in frame i, with $\dot{P}^i = 0$, the velocity in frame j becomes

$$\dot{P}^j = \dot{H}^j_i P^i + \cancelto{0}{H^j_i \dot{P}^i} \tag{A-9}$$

A twist is defined as

$$\widetilde{T}_i^{j,j} \coloneqq \dot{H}_i^j H_j^i \Rightarrow \dot{H}_i^j = \widetilde{T}_i^{j,j} H_i^j \tag{A-10}$$

Then

$$\dot{P}^j = \dot{H}_i^j P^i = \widetilde{T}_i^{j,j} H_i^j P^i = \widetilde{T}_i^{j,j} P^j \tag{A-11}$$

A twist consists of the angular velocities and the translational velocities and can be written in both tilde and normal form

$$T \coloneqq \begin{bmatrix} \omega \\ v \end{bmatrix} \Rightarrow \widetilde{T} = \begin{bmatrix} \widetilde{\omega} & v \\ 0 & 0 \end{bmatrix} \tag{A-12}$$

Where ω is the angular velocity and v the linear velocity. Twists can be written in different forms regarding the coordinate frame from which the rotation is observed. The twist of frame i with respect to frame j seen from frame i and j respectively is defined as:

$$\widetilde{T}_i^{i,j} = H_j^i \dot{H}_i^j \quad \text{and} \quad \widetilde{T}_i^{j,j} = \dot{H}_i^j H_j^i \tag{A-13}$$

The change of coordinates for twists is defined as

$$\widetilde{T}_i^{j,j} = H_i^j \widetilde{T}_i^{i,j} H_j^i \tag{A-14}$$

Or, when using the normal form

$$T_i^{j,j} = Ad_{H_i^j} T_i^{i,j} \tag{A-15}$$

With the adjoint notation of H_i^j defined as

$$Ad_{H_i^j} \coloneqq \begin{bmatrix} R_i^j & 0 \\ \widetilde{p}_i^j R_i^j & R_i^j \end{bmatrix} \tag{A-16}$$

A-1-3 Forces on a rigid body: Wrenches

We now know that twists are the generalization of velocities. In order to find the generalization of forces one should look at the definition of power due to a force and velocity

$$P = fv \tag{A-17}$$

Where f is a row vector and v a column vector. Now, extending to six dimensions of motion, power becomes

$$P = WT \tag{A-18}$$

Where T is the twit and W the wrench defined as

$$W = \begin{bmatrix} \tau & f \end{bmatrix} \tag{A-19}$$

The power definition only holds when both the twist and wrench are defined in the same coordinate system. The conservation of power allows us to transform wrenches from one coordinate frame to the other as follows

$$W^j T_j^{j,i} = W^j Ad_{H_i^j} T_j^{i,i} = \left(Ad_{H_i^j}^T (W^j)^T \right)^T T_j^{i,i} = W^i T_j^{i,i} \tag{A-20}$$

And thus

$$(W^i)^T = Ad_{H_i^j}^T (W^j)^T \tag{A-21}$$

A-1-4 Direct kinematics

Consider the definition for twists

$$\widetilde{T}_i^{j,j} := \dot{H}_i^j H_j^i \Rightarrow \dot{H}_i^j = \widetilde{T}_i^{j,j} H_i^j \tag{A-22}$$

With $\widetilde{T}_i^{j,j}$ constant the solution to the differential equation is

$$H_i^j(t) = e^{\widetilde{T}_i^{j,j} t} H_i^j(0) \tag{A-23}$$

Now, define unit twists as twists with unit length vector for rotation or translation when no rotation is present. Unit twists and vectors are indicated using the hat notation.

$$\widehat{T} = \begin{bmatrix} \widehat{\omega} \\ * \end{bmatrix} \quad \text{, and} \quad \widehat{T} = \begin{bmatrix} 0 \\ \widehat{v} \end{bmatrix} \tag{A-24}$$

A unit twist defines the degree of freedom of an actuator and may be multiplied with a scalar to obtain the twist of an actuator

$$T = \widehat{T}\dot{q}_j \tag{A-25}$$

The basic joints are defined as

$$\text{Rotational joint:} \qquad \widehat{T} = \begin{pmatrix} \widehat{\omega} \\ r \wedge \widehat{\omega} \end{pmatrix} \tag{A-26}$$

$$\text{Translational joint:} \qquad \widehat{T} = \begin{pmatrix} 0 \\ \widehat{v} \end{pmatrix} \tag{A-27}$$

The transformation matrix at joint level becomes

$$H_i^j(q_j) = e^{\widetilde{\widehat{T}}_i^{j,j} \, q_j} H_i^j(0) \tag{A-28}$$

Where q_j is the generalized coordinate for the actuator which may represent a rotation or a translation. The chain rule for transformation matrices dictates

$$H_n^0 = H_1^0 H_2^1 \dots H_n^{n-1} \tag{A-29}$$

And thus, using Brockett's exponential formula, for a system with three actuators the transformation matrix becomes

$$H_3^0(q_1, q_2, q_3) = e^{\widetilde{\widehat{T}}_1^{0,0} \, q_1} \, H_1^0(0) \, e^{\widetilde{\widehat{T}}_2^{1,1} \, q_2} \, H_2^1(0) \, e^{\widetilde{\widehat{T}}_3^{2,2} \, q_3} \, H_3^2(0) \tag{A-30}$$

Adding identity matrices and rewriting gives

$$H_3^0(q_1, q_2, q_3) = e^{\widetilde{\widehat{T}}_1^{0,0} \, q_1} \, H_1^0(0) \, e^{\widetilde{\widehat{T}}_2^{1,1} \, q_2} \overbrace{H_0^1(0) \, H_1^0(0)}^{I} H_2^1(0) \, e^{\widetilde{\widehat{T}}_3^{2,2} \, q_3} \overbrace{H_0^2(0) \, H_2^0(0)}^{I} H_3^2(0) \tag{A-31}$$

$$H_3^0(q_1, q_2, q_3) = e^{\widetilde{\widehat{T}}_1^{0,0} \, q_1} \underbrace{H_1^0(0) \, e^{\widetilde{\widehat{T}}_2^{1,1} \, q_2} H_0^1(0)}_{e^{\widetilde{\widehat{T}}_2^{0,1} \, q_2}} \underbrace{H_1^0(0) \, H_2^1(0) \, e^{\widetilde{\widehat{T}}_3^{2,2} \, q_3} H_0^2(0)}_{e^{\widetilde{\widehat{T}}_3^{0,2} \, q_3}} \underbrace{H_2^0(0) \, H_3^2(0)}_{H_3^0(0)} \tag{A-32}$$

$$H_3^0(q_1, q_2, q_3) = e^{\widetilde{\widehat{T}}_1^{0,0} \, q_1} \, e^{\widetilde{\widehat{T}}_2^{0,1} \, q_2} \, e^{\widetilde{\widehat{T}}_3^{0,2} \, q_3} \, H_3^0(0) \tag{A-33}$$

Where the twists in the exponentials are the unit twists of the actuators in the reference configuration with $q_1 = q_2 = q_3 = 0$ and $H_3^0(0)$ the transformation matrix in the reference configuration.

A-1-5 Geometrical Jacobian

The geometrical jacobian relates the actuator velocities to the tip speed and can be used in the controller. The Jacobian is derived using the definition for the twist.

$$\widetilde{T}_3^{0,0} = \dot{H}_3^0 H_0^3 \tag{A-34}$$

Using the chain rule for transformation matrices, the twist becomes

$$\widetilde{T}_3^{0,0} = \left(H_1^0 \dot{H}_2^1 H_3^2\right)\left(H_2^3 H_1^2 H_0^1\right) \tag{A-35}$$
$$\widetilde{T}_3^{0,0} = \dot{H}_1^0 H_0^1 + H_1^0 \dot{H}_2^1 H_1^2 H_0^1 + H_2^0 \dot{H}_3^2 H_2^3 H_0^2 \tag{A-36}$$
$$\widetilde{T}_3^{0,0} = \widetilde{T}_1^{0,0} + H_1^0 \widetilde{T}_2^{1,1} H_0^1 + H_2^0 \widetilde{T}_3^{2,2} H_0^2 \tag{A-37}$$

And written in the normal notation using adjoint transformation matrices

$$T_3^{0,0} = T_1^{0,0} + Ad_{H_1^0} T_2^{1,1} + Ad_{H_2^0} T_3^{2,2} \tag{A-38}$$
$$T_3^{0,0} = T_1^{0,0} + T_2^{0,1} + T_3^{0,2} \tag{A-39}$$

And, from the definition of unit twists and generalized coordinates for actuators, the twist can be written as

$$T_3^{0,0} = \widehat{T}_1^{0,0}\dot{q}_1 + \widehat{T}_2^{0,1}\dot{q}_2 + \widehat{T}_3^{0,2}\dot{q}_3 \tag{A-40}$$
$$T_3^{0,0} = J(q)\dot{q} \tag{A-41}$$

With

$$J\left(q\right) = \begin{pmatrix} \widehat{T}_1^{0,0} & \widehat{T}_2^{0,1} & \widehat{T}_3^{0,2} \end{pmatrix} \tag{A-42}$$
$$q = \begin{pmatrix} q_1 & q_2 & q_3 \end{pmatrix}^T \tag{A-43}$$

Now that the joint velocities are related to the end effector twist, a wrench on the tip can be related to torques and forces in the actuators using conservation of energy

$$\tau^T = J^T(q)\left(W^{0,n}\right)^T \tag{A-44}$$

A-1-6 Change of coordinates for inertia matrices

Using the twist and wrench notation as defined above, the principal inertia tensor of a rigid body i is the 6x6 matrix

$$\mathfrak{T}^i = \begin{pmatrix} J_i & 0 \\ 0 & m_i I \end{pmatrix} \tag{A-45}$$

Where m_i is the mass of body i and J_i the rotational inertia of body i defined as

$$J_i = \begin{pmatrix} j_x & 0 & 0 \\ 0 & j_y & 0 \\ 0 & 0 & j_z \end{pmatrix} \tag{A-46}$$

The relation to standard formulation of kinetic energy is shown using the velocity twists defining the kinetic energy as

$$T^* = \frac{1}{2} \left(T_i^{i,0}\right)^T \mathfrak{T}^i T_i^{i,0} \tag{A-47}$$

$$= \frac{1}{2} m_i \left\| v_i^{i,0} \right\|^2 + \frac{1}{2} j_x \omega_x^2 + \frac{1}{2} j_y \omega_y^2 + \frac{1}{2} j_z \omega_z^2 \tag{A-48}$$

The principal inertia tensor is defined in a reference frame aligned along the principal inertia axis with the origin in the center of gravity of the body. Transformation to frame k is carried out using the adjoint notation as follows

$$\mathfrak{T}^{k,i} = Ad_{H_k^i}^T \, \mathfrak{T}^i Ad_{H_k^i} \tag{A-49}$$

Appendix B

Robot Dynamics

B-1 Euler-Lagrangian dynamics

With the generalized coordinates and the generalized forces on the actuators defined, the dynamics of the system will be determined using the Euler-Lagrange equations. Using the kinetic co-energy $T^*(q, \dot{q})$ and potential energy $V(q)$ as function of the generalized coordinates q. Hamilton's Principle of least action dictates that the following function is minimized

$$\int_{t_1}^{t_2} \mathcal{L}\left(q\left(t\right), \dot{q}\left(t\right)\right) dt \tag{B-1}$$

With the Lagrangian

$$\mathcal{L}\left(q, \dot{q}\right) \coloneqq T^*\left(q, \dot{q}\right) - V(q) \tag{B-2}$$

Which leads to the well known Euler-Lagrange equations

$$\frac{d}{dt}\left(\frac{\partial \mathcal{L}}{\partial \dot{q}}\right) - \frac{\partial \mathcal{L}}{\partial q} = 0 \tag{B-3}$$

When the input is τ such that the power provided to the system is $P = \tau \dot{q}$ the equations become

$$\frac{d}{dt}\left(\frac{\partial \mathcal{L}}{\partial \dot{q}}\right) - \frac{\partial \mathcal{L}}{\partial q} = \tau^T \tag{B-4}$$

B-1-1 Kinetic co-energy

We have seen that for body i the kinetic co-energy is expressed as

$$T_i^* = \frac{1}{2} \left(T_i^{i,0}\right)^T \mathfrak{T}^i T_i^{i,0} \tag{B-5}$$

The function that gives the twist of body i as function of the generalized coordinates $\dot{q}$ is

$$T_i^{0,0} = J_i(q)\dot{q} \tag{B-6}$$

With

$$J_i\left(q\right) \coloneqq \begin{pmatrix} \widehat{T}_1^{0,0} & \dots & \widehat{T}_i^{0,(i-1)} & 0 & \dots & 0 \end{pmatrix} \tag{B-7}$$

Since rotations of bodies $i+1, \dots, n$ do not count towards the rotation of body i directly. Then, using

$$T_i^{i,0} = Ad_{H_0^i} T_i^{0,0} \tag{B-8}$$

The equation for kinetic co-energy of body i becomes

$$T_i^* = \frac{1}{2}\, \dot{q}^T \underbrace{J_i^T(q) Ad_{H_0^i}^T \mathfrak{T}^i Ad_{H_0^i} J_i(q)}_{M_i(q)}\, \dot{q} \tag{B-9}$$

The total kinetic co-energy of the whole system is

$$T^*(q, \dot{q}) = \frac{1}{2}\dot{q}^T M(q)\dot{q} \tag{B-10}$$

With

$$M\left(q\right) \coloneqq \sum_i M_i(q) \tag{B-11}$$

B-1-2 Potential energy

The potential energy of body i is defined using the standard formulation for potential energy due to gravitational pull. The z axis in the zero frame is defined as being the vertical axis. And thus the potential becomes

$$V_i(q) = m_i g h = m_i g \begin{pmatrix} 0 & 0 & 1 & 0 \end{pmatrix} P_g^0 = \tag{B-12}$$

$$= m_i g \begin{pmatrix} 0 & 0 & 1 & 0 \end{pmatrix} H_i^0 P_g^i \tag{B-13}$$

With P_g^i the location of the center of gravity of body i in reference frame i.The total potential energy is

$$V(q) = \sum_i V_i(q) \tag{B-14}$$

The gravity vector which relates the forces on the actuators to the generalized coordinates is

$$G(q) = \frac{\partial V(q)}{\partial q} \tag{B-15}$$

B-1-3 Result of Euler-Lagrange: Robot's equations

Remember the Euler-Lagrange equations

$$\frac{d}{dt}\left(\frac{\partial \mathcal{L}}{\partial \dot{q}}\right) - \frac{\partial \mathcal{L}}{\partial q} = \tau^T \tag{B-16}$$

With the Lagrangian

$$\mathcal{L}(q, \dot{q}) = \frac{1}{2}\dot{q}^T M(q)\, \dot{q} - V(q) \tag{B-17}$$

For easier calculation, write the first term as a sum

$$\mathcal{L}(q, \dot{q}) = \frac{1}{2}\sum_{i,j=1}^{n} M_{ij}(q)\dot{q}_i\dot{q}_j - V(q) \tag{B-18}$$

With n the dimension of q. The elements of the Euler-Lagrange equations become

$$\frac{d}{dt}\left(\frac{\partial \mathcal{L}}{\partial \dot{q}_i}\right) = \frac{d}{dt}\left(\sum_{j=1}^{n} M_{ij}\dot{q}_j\right) = \sum_{j=1}^{n}\left(M_{ij}\ddot{q}_j + \dot{M}_{ij}\dot{q}_j\right) \tag{B-19}$$

$$-\frac{\partial \mathcal{L}}{\partial q_i} = -\frac{1}{2}\sum_{j,k=1}^{n}\frac{\partial M_{kj}}{\partial q_i}\dot{q}_k\dot{q}_j + \frac{\partial V}{\partial q_i} \tag{B-20}$$

Express

$$\dot{M}_{ij} = \sum_{k=1}^{n}\frac{\partial M_{ij}}{\partial q_k}\dot{q}_k \tag{B-21}$$

The Euler-Lagrange equations become

$$\sum_{j=1}^{n} M_{ij}\ddot{q}_j + \sum_{j,k=1}^{n}\left(\frac{\partial M_{ij}}{\partial q_k}\dot{q}_j\dot{q}_k - \frac{1}{2}\frac{\partial M_{kj}}{\partial q_i}\ \dot{q}_k\dot{q}_j\right) + \frac{\partial V}{\partial q_i} = \tau_i \tag{B-22}$$

Inverting the indices j with k enables us to write

$$\sum_{j,k=1}^{n}\frac{\partial M_{ij}}{\partial q_k}\dot{q}_j\dot{q}_k = \sum_{j,k=1}^{n}\frac{\partial M_{ik}}{\partial q_j}\dot{q}_j\dot{q}_k \tag{B-23}$$

And thus

$$\sum_{j,k=1}^{n}\frac{\partial M_{ij}}{\partial q_k}\dot{q}_j\dot{q}_k = \frac{1}{2}\sum_{j,k=1}^{n}\left(\frac{\partial M_{ij}}{\partial q_k} + \frac{\partial M_{ik}}{\partial q_j}\right)\dot{q}_j\dot{q}_k \tag{B-24}$$

The Euler-Lagrange equations can be written as

$$\sum_{j=1}^{n} M_{\mathrm{ij}}\ddot{q}_j + \sum_{j,k=1}^{n}\underbrace{\frac{1}{2}\left(\frac{\partial M_{\mathrm{ij}}}{\partial q_k} + \frac{\partial M_{\mathrm{ik}}}{\partial q_j} - \frac{\partial M_{\mathrm{kj}}}{\partial q_i}\right)}_{\Gamma_{i,j,k}}\dot{q}_j\dot{q}_k + \frac{\partial V}{\partial q_i} = \tau_i \tag{B-25}$$

In which the Christoffels symbols can be found as

$$\Gamma_{i,j,k} \coloneqq \frac{1}{2}\left(\frac{\partial M_{\mathrm{ij}}}{\partial q_k} + \frac{\partial M_{\mathrm{ik}}}{\partial q_j} - \frac{\partial M_{\mathrm{kj}}}{\partial q_i}\right) \tag{B-26}$$

Define the matrix which represents the centrifugal and Coriolis forces as

$$C_{i,j}\left(q,\dot{q}\right)=\sum_{k=1}^{n}\Gamma_{i,j,k}\ \dot{q}_k \tag{B-27}$$

Then, the final dynamic equations can be written as

$$M\left(q\right)\ddot{q}+C\left(q,\dot{q}\right)\dot{q}+G\left(q\right)=\tau^T \tag{B-28}$$

Motor torques, interaction forces, and friction forces all enter the equation as τ.

B-2 Non inertial frame of reference

Up to this point all dynamics have been defined in an inertial frame of reference. However, the purpose of this model is to simulate the dynamics of a gangway mounted on a moving vessel. Therefore, ship movement is introduced. The ship is able to move in 6 degrees of freedom. Translational movement heave, surge, sway and rotational movement roll, pitch, and yaw. Defined in transformation matrix H_0^e. The time derivative of the ship movement is defined as velocity of frame 0 with respect to frame e as seen from frame 0. The twist notation is $T_0^{0,e}$. Then, the total energy of body i is

$$T_i^*=\frac{1}{2}\left(T_i^{i,e}\right)^T\mathfrak{T}^iT_i^{i,e} \tag{B-29}$$

$$=\frac{1}{2}\left(T_i^{0,e}\right)^T Ad_{H_0^i}^T\mathfrak{T}^iAd_{H_0^i}T_i^{0,e} \tag{B-30}$$

Where

$$T_i^{0,e}=T_i^{0,0}+T_0^{0,e}=J_i\left(q\right)\dot{q}+T_0^{0,e} \tag{B-31}$$

Then, the equation for the total energy of body i becomes

$$T_i^*=\frac{1}{2}\ \left(J_i\left(q\right)\dot{q}+T_0^{0,e}\right)^T Ad_{H_0^i}^T\mathfrak{T}^iAd_{H_0^i}\left(J_i\left(q\right)\dot{q}+T_0^{0,e}\right) \tag{B-32}$$

$$T_i^*=\frac{1}{2}\ \left[\left(T_0^{0,e}\right)^T\quad\dot{q}^T\right]M_i\left(q\right)\begin{bmatrix}T_0^{0,e}\\ \dot{q}\end{bmatrix}=\frac{1}{2}\ v^tM_i\left(q\right)v \tag{B-33}$$

Where v is the state vector $v=\begin{bmatrix}T_0^{0,e}\\ \dot{q}\end{bmatrix}$ and $M_i\left(q\right)$ is

$$M_i(q) = \begin{bmatrix} Ad_{H_0^i}^T \mathfrak{T}^i Ad_{H_0^i} & Ad_{H_0^i}^T \mathfrak{T}^i Ad_{H_0^i} J_i \\ J_i^T Ad_{H_0^i}^T \mathfrak{T}^i Ad_{H_0^i} & J_i^T Ad_{H_0^i}^T \mathfrak{T}^i Ad_{H_0^i} J_i \end{bmatrix} \tag{B-34}$$

Now, the robot's equation becomes

$$\begin{bmatrix} M_{TT} & M_{qT}^T \\ M_{qT} & M_{qq} \end{bmatrix} \begin{bmatrix} \dot{T}_0^{0,e} \\ \ddot{q} \end{bmatrix} + \begin{bmatrix} C_{TT} & C_{Tq} \\ C_{qT} & C_{qq} \end{bmatrix} \begin{bmatrix} T_0^{0,e} \\ \dot{q} \end{bmatrix} = \begin{bmatrix} W^0 \\ \tau \end{bmatrix} \tag{B-35}$$

Where W^0 is the external wrench on the base. The forces in the actuators are relevant for the dynamics of the gangway and thus the robot equation reduces to

$$M_{qq}\ddot{q} + C_{qq}\dot{q} + M_{qT}\dot{T}_0^{0,e} + C_{qT}T_0^{0,e} = \tau \tag{B-36}$$

This partially separates the inertial dynamics with the non inertial dynamics. C_{qq} still depends on $T_0^{0,e}$. When $\dot{T}_0^{0,e}$ and $T_0^{0,e}$ are zero, the equation above reduces to the inertial dynamics. The matrices C_{qq} and C_{qT} can be written as

$$C_{qq} = \sum_{k=1}^{n} \frac{\partial M_{qq}}{\partial q_k}\dot{q}_k - \frac{1}{2}\frac{\partial^T}{\partial q}\left(\begin{bmatrix} M_{qT} & M_{qq}^T \end{bmatrix} \begin{bmatrix} T_0^{0,e} \\ \dot{q} \end{bmatrix}\right) \tag{B-37}$$

$$C_{qT} = \sum_{k=1}^{n} \frac{\partial M_{qT}}{\partial q_k}\dot{q}_k - \frac{1}{2}\frac{\partial^T}{\partial q}\left(\begin{bmatrix} M_{TT} & M_{qT}^T \end{bmatrix} \begin{bmatrix} T_0^{0,e} \\ \dot{q} \end{bmatrix}\right) \tag{B-38}$$

The potential energy of body i will be defined in the earth frame instead of the 0 frame. With the z axis being the vertical axis.

$$V_i(q, H_0^e) = m_i q h = m_i g \begin{pmatrix} 0 & 0 & 1 & 0 \end{pmatrix} P_g^e = \tag{B-39}$$

$$= m_i g \begin{pmatrix} 0 & 0 & 1 & 0 \end{pmatrix} H_o^e H_i^0 P_g^i \tag{B-40}$$

The total potential energy and the gravitational vector are defined as

$$V(q, H_0^e) = \sum_i V_i(q) \tag{B-41}$$

$$G(q, H_0^e) = \frac{\partial V(q)}{\partial q} \tag{B-42}$$

The gravitational vector enters the robot equation in the same way as before. Which produces the final robot equation

$$M_{qq}(q)\ddot{q} + C_{qq}\left(q, \dot{q}, H_0^e, T_0^{0,e}\right)\dot{q} + M_{qT}(q)\dot{T}_0^{0,e} + C_{qT}\left(q, \dot{q}, H_0^e, T_0^{0,e}\right)T_0^{0,e} + G(q, H_0^e) = \tau \tag{B-43}$$

Appendix C

Flexible Robotics

C-1 Modal analysis of deflections

The 3D model includes kinematics and dynamics of the Motion Compensated Gangway (MCG) in combination with ship movements, actuator properties, interaction with the environment. This appendix describes the methods that have been used to model the structural deflections of the Gangway. The exaggerated deformations which are modelled are shown in Figure C-1.

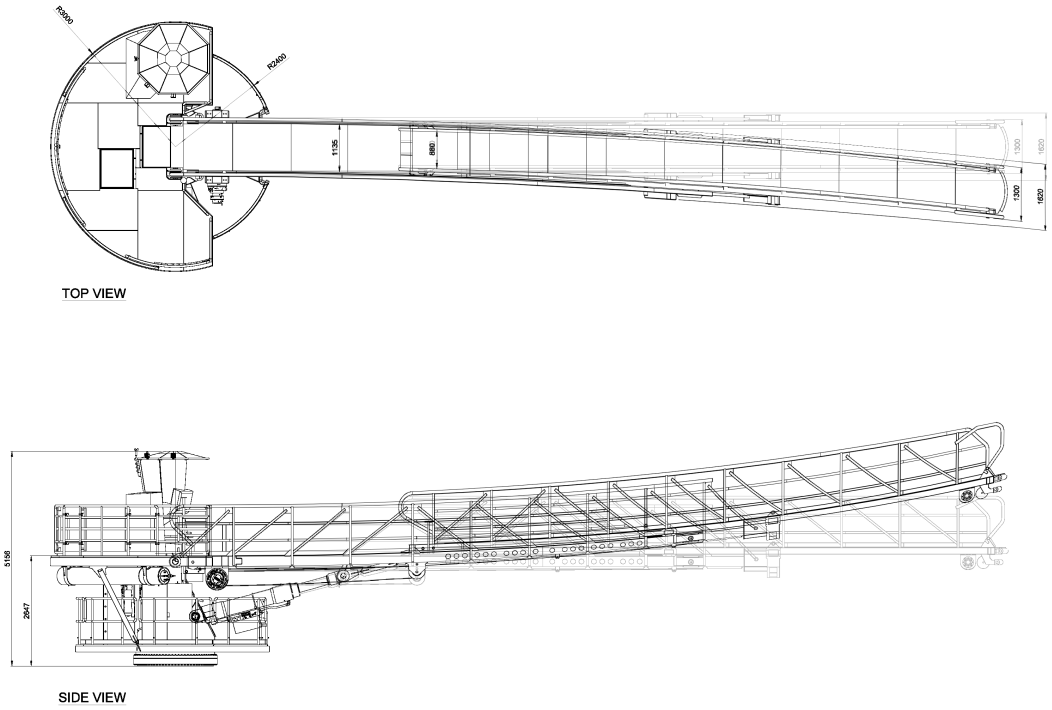

Figure C-1: Modelled deformations of Barge Master Gangway.

C-1-1 Methods for flexible dynamics

The dynamics of flexible beams can be represented using a nonlinear dynamical system with infinite dimensions [24]. For simulation properties this is not feasible, therefore three approaches have been used: lumped parameters, assumed modes and finite element method [24].

For the lumped parameters method the beam is divided in a finite number of rigid beams connected by pseudo joints. This method is rarely used because of the difficulty in estimating the spring constants in the pseudo joints and achieving the desired accuracy.

The assumed modes method uses the spatial mode eigenfunctions and time varying vibrational modes [24]. In order to achieve the desired accuracy the series of vibrational modes can be truncated down to a few vibrational modes. The spatial modes are determined using the boundary conditions for the beam.

In the finite element method the flexible beam is divided into smaller sections. For all sections the local deformation is described in element-wise basis functions. This usually requires more computational effort than the assumed modes method since more sections than modes are needed in order to achieve the same accuracy [24].

The assumed modes method is recommended for single link flexible manipulators with uniform cross sectional geometries. Also, the assumed modes method is recommended for use in numerical simulations [25]. The finite element method is recommended in cases where multilink manipulators with complex cross sectional geometries are used. This however is not the case here [25].

C-1-2 Assumed modes

For the dynamic modeling of the structural bending of the Gangway the assumed modes method is used. The following assumptions are made:

1. The Gangway is modeled as a slender *Euler-Bernoulli* beam with uniform geometric characteristics and homogeneous mass distribution.
2. The beam is clamped to a rigid hub of the transfer deck producing two torques τ.
3. The basis of the gangway (hub) has zero inertia for vertical deformation.
   (a) This could be added for horizontal deformation (due to transfer deck inertia)
4. The beam is flexible in the lateral directions only.
5. The beam is stiff in axial direction and torsion.
6. Deformations are small and are in the elastic domain.

Alessandro De Luca proposes a system with one flexible link in [26]. The dynamic model proposed by De Luca is derived from Hamiltons principle and shown in equations C-1 to C-3.

$$I_t\ddot{\theta}_c(t) + \rho \int_0^l x\,\ddot{w}(x,t)\,dx = \tau(t) \tag{C-1}$$

$$EIw''''(x,t) + \rho\ddot{w}(x,t) + \rho x\ddot{\theta}_c(t) = 0 \tag{C-2}$$

$$w(0,t) = w'(0,t) = 0, \quad w''(l,t) = w'''(l,t) = 0 \tag{C-3}$$

In which ρ is the weight per unit length of the beam, EI the flexural rigidity, l the beam length, and I_t the total inertia of the beam at the base. Furthermore $\theta_c(t)$ is the hub rotation and the link deformation is $w(x,t)$ with $x \in [0,l]$. Equation C-3 are the clamped-free boundary conditions at the two ends of the beam. For the analysis, a distinction is made between the motor angle θ_c, the undeformed angle which crosses the beam center of gravity θ and the angle to the beam tip θ_t shown in figure C-2.

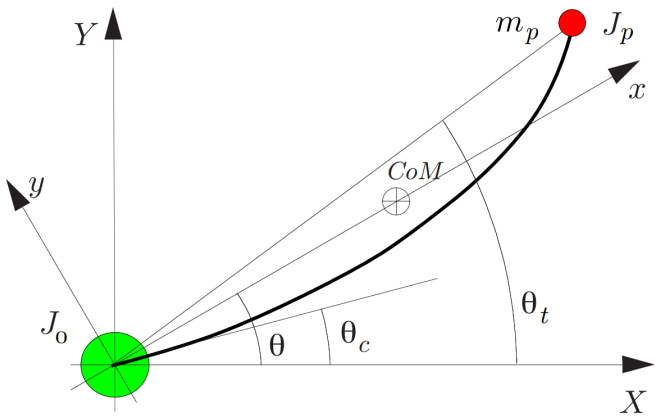

Figure C-2: Definition of the used angles in the deformed beam. [6]

The deformation $w(x,t)$ is a function of space and time. The method of separation of variables is used in order to solve the partial differential equations and boundary conditions given in equations C-1 to C-3. Saad and Wang [27, 28] describe the separation of variables as follows:

$$w(x,t) = \sum_{i=1}^{m_e} \phi_i(x)\delta_i(t) = \phi^T(x)\delta(t) \tag{C-4}$$

Here, the orthonormal shape functions are described by $\phi_i(x)$ and the time varying generalized coordinate $\delta_i(t)$ with index $i = [1, 2, \ldots, m_e]$ denoting the normal modes of vibration. The shape functions are of the form [29]

$$\phi_i(x) = A_i \sin\left(\beta_i \frac{x}{l}\right) + B_i \cos\left(\beta_i \frac{x}{l}\right) + C_i \sinh\left(\beta_i \frac{x}{l}\right) + D_i \cosh\left(\beta_i \frac{x}{l}\right) \tag{C-5}$$

With the constants A_i to D_i determined by the boundary conditions, described by Axisa [29]. The values for β_i are determined by the characteristic equations shown in equation C-6 [29].

$$\begin{aligned} 1 + \cos(\beta)\cosh(\beta) &= 0 \qquad \text{(clamped-free)} \\ \cos(\beta)\sinh(\beta) - \sin(\beta)\cosh(\beta) &= 0 \qquad \text{(pinned-free)} \end{aligned} \tag{C-6}$$

The corresponding values for the first two modes are shown in table C-1.

Table C-1: β_i values for first two modes of shape functions

β_i	Mode 1	Mode 2
Clamped-free	1.8751	4.6941
Pinned-free	3.9266	7.0686

A finite discrete model is obtained by assuming a finite amount of eigenmodes m_e. The first two shape modes of the *Euler-Bernoulli* beam for both clamped-free and pinned-free are derived [29] and normalized as described by Wang [28] as shown in equation C-7. De Luca [6] states that normalization can be done to any integral of $\phi_i(x)$, it is later shown that this normalization has a large effect on the deflection.

$$\int_0^l \phi_i(x)^2 \, dx = 1 \tag{C-7}$$

The eigenfrequencies for each mode shape are a function of β and the physical properties as shown in equation C-8 [26]

$$\omega_i = \sqrt{\frac{EI\beta_i^4}{\rho l^4}} \tag{C-8}$$

These normalized orthogonal shape functions are shown for a Gangway length of $27m$ in figure C-3 and C-4.

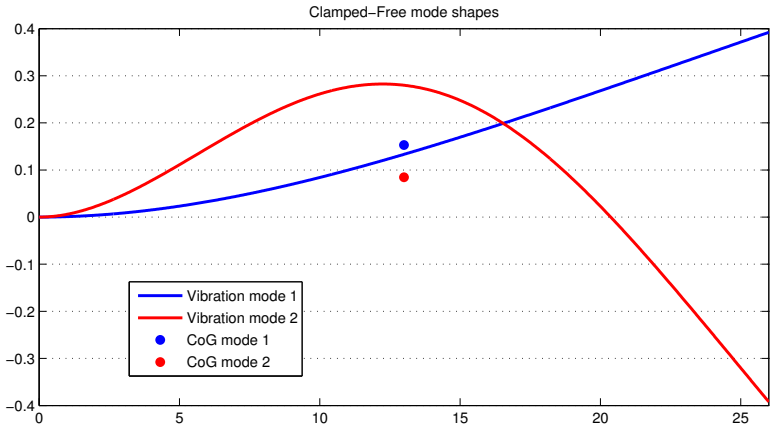

Figure C-3: The first two orthonormal shape modes for a clamped-free beam.

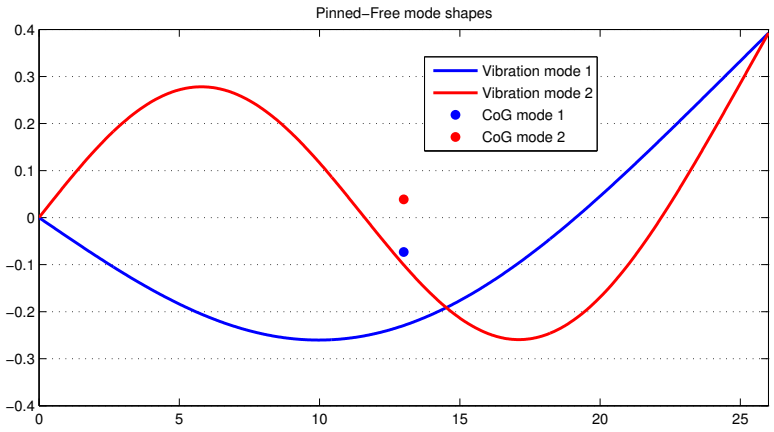

Figure C-4: The first two orthonormal shape modes for a pinned-free beam.

C-1-3 Clamped-free

Both Saad [30, 31] and De Luca [26, 6] give equations for the flexible dynamics with the actuator angles as states, and thus deformations defined in the coordinate system tangent to the base of the gangway. These methods define the kinetic and potential energy of the deformed clamped beam. Then, the Euler-Langrange equations are defined as:

$$\frac{d}{dt}\left(\frac{\partial L}{\partial \dot{\theta_c} i}\right) - \frac{\partial L}{\partial \theta_c i} = \tau_i \qquad i = 1, \ldots, N \tag{C-9}$$

$$\frac{d}{dt}\left(\frac{\partial L}{\partial \dot{\delta}_{ij}}\right) - \frac{\partial L}{\partial \delta_{ij}} = 0 \qquad j = 1, \ldots, m_e \quad i = 1, \ldots, N \tag{C-10}$$

The dynamic model becomes:

$$\begin{bmatrix} M_{\theta\theta}(\theta_c,\delta) & M_{\theta\delta}(\theta_c,\delta) \\ M_{\theta\delta}^T(\theta_c,\delta) & M_{\delta\delta}(\theta_c,\delta) \end{bmatrix} \begin{bmatrix} \ddot{\theta}_c \\ \ddot{\delta} \end{bmatrix} + \begin{bmatrix} C_{\theta\theta}(\theta_c,\delta,\dot{\theta}_c,\dot{\delta}) & C_{\theta\delta}(\theta_c,\delta,\dot{\theta}_c,\dot{\delta}) \\ C_{\theta\delta}(\theta_c,\delta,\dot{\theta}_c,\dot{\delta}) & C_{\delta\delta}(\theta_c,\delta,\dot{\theta}_c,\dot{\delta}) \end{bmatrix} \begin{bmatrix} \dot{\theta}_c \\ \dot{\delta} \end{bmatrix} + \\ + \begin{bmatrix} g_\theta(\theta_c,\delta) \\ g_\delta(\theta_c,\delta) \end{bmatrix} + \begin{bmatrix} 0 \\ D\dot{\delta} + K\delta \end{bmatrix} = \begin{bmatrix} \tau \\ 0 \end{bmatrix} \tag{C-11}$$

Instead of using the rigid dynamics calculated using concentrated masses, all energies are determined assuming uniform distributed mass over the length of the beam. Below this method will be worked out for a one degree of freedom beam with the first flexible mode. Eventually the method will be used in three dimensions with the y-axis pointing towards the paper. Therefore, positive rotation is defined in downward direction. See Figure C-5.

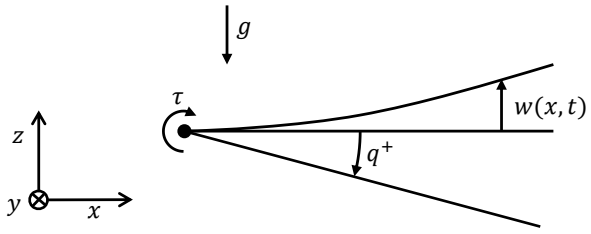

Figure C-5: Definition of rotations and deformations used in method Saad.

Here only the x and z axis are relevant and the y axis will be omitted in notation. The location of a point on the beam is defined in the earth reference frame as

$$p(x) = \begin{bmatrix} x\cos(q) + w(x)\sin(q) \\ -x\sin(q) + w(x)\cos(q) \end{bmatrix} \tag{C-12}$$

The gravity vector is defined as

$$\vec{g} = \begin{bmatrix} 0 \\ g \end{bmatrix} \tag{C-13}$$

The potential energy is a combination of elastic energy due to internal forces and gravitational potential energy.

$$V = \underbrace{\frac{1}{2}EI\int_0^l w''(x)^2\,dx}_{\text{Elastic}} + \underbrace{\int_0^l \rho\vec{g}^T p(x)\,dx}_{\text{Gravitational}} \tag{C-14}$$

Or

$$V = \frac{1}{2}EI \int_0^l w''(x)^2 \, dx - g \int_0^l \rho x \sin(q) \, dx + g \int_0^l \rho w(x) \cos(q) \, dx \tag{C-15}$$

Applying the separation of variables for the beam deformation, equation C-15 becomes

$$V = \frac{1}{2}EIq_f^2 \int_0^l (\phi'')^2 \, dx - \frac{1}{2}\rho g l^2 \sin(q) + \rho g \int_0^l \phi \, dx \, q_f \cos(q) \tag{C-16}$$

The kinetic energy equation uses the velocity of a point in the beam defined in the reference frame of the base of the beam, then the velocity becomes

$$v(x) = \begin{bmatrix} -\dot{q}w \\ \dot{w} - x\dot{q} \end{bmatrix} \tag{C-17}$$

The kinetic energy of the beam is

$$T = \frac{1}{2} \int_0^l \rho v(x)^T v(x) \, dx \tag{C-18}$$

Or

$$T = \frac{1}{2} \int_0^l \rho \dot{q}^2 w^2 \, dx + \frac{1}{2} \int_0^l \rho \left(\dot{w}^2 - 2x\dot{q}\dot{w} + x^2\dot{q}^2 \right) \, dx \tag{C-19}$$

Again, by applying the separation of variables for the beam deformation, equation C-19 becomes

$$T = \frac{1}{2}\rho \dot{q}^2 q_f^2 \int_0^l \phi^2 \, dx + \frac{1}{2}\rho \dot{q}_f^2 \int_0^l \phi^2 \, dx - \rho \dot{q}\dot{q}_f \int_0^l x\phi \, dx + \frac{1}{2}\rho \frac{1}{3} l^3 \dot{q}^2 \tag{C-20}$$

The kinetic and potential energy are combined to form the Lagrangian

$$L = T - V \tag{C-21}$$

Which becomes

$$L = \frac{1}{2}\rho \dot{q}^2 q_f^2 \int_0^l \phi^2 \, dx + \frac{1}{2}\rho \dot{q}_f^2 \int_0^l \phi^2 \, dx - \rho \dot{q}\dot{q}_f \int_0^l x\phi \, dx + \frac{1}{2}\rho \frac{1}{3} l^3 \dot{q}^2 \tag{C-22}$$

$$-\frac{1}{2}EIq_f^2 \int_0^l (\phi'')^2 \, dx + \frac{1}{2}\rho g l^2 \sin(q) - \rho g \int_0^l \phi \, dx \, q_f \cos(q) \tag{C-23}$$

The Lagrange equations are applied as follows

$$\frac{d}{dt}\left(\frac{\partial L}{\partial \dot{q}}\right) - \frac{\partial L}{\partial q} = \tau \tag{C-24}$$

$$\frac{d}{dt}\left(\frac{\partial L}{\partial \dot{q}_f}\right) - \frac{\partial L}{\partial q_f} = 0 \tag{C-25}$$

The steps which are used to calculate the result of the Lagrange equations are shown in equations C-26 to C-28 for the rigid dynamics and C-29 to C-31 for the flexible dynamics.

$$\frac{\partial L}{\partial \dot{q}} = \rho \dot{q} q_f^2 \int_0^l \phi^2 \, dx - \rho \dot{q}_f \int_0^l x\phi \, dx + \rho \frac{1}{3} l^3 \dot{q} \tag{C-26}$$

$$\frac{d}{dt}\left(\frac{\partial L}{\partial \dot{q}}\right) = \rho \ddot{q} q_f^2 \int_0^l \phi^2 \, dx + 2\rho \dot{q} q_f \dot{q}_f \int_0^l \phi^2 \, dx - \rho \ddot{q}_f \int_0^l x\phi \, dx + \rho \frac{1}{3} l^3 \ddot{q} \tag{C-27}$$

$$-\frac{\partial L}{\partial q} = -\frac{1}{2}\rho g l^2 \cos(q) - \rho g \int_0^l \phi \, dx \, q_f \sin(q) \tag{C-28}$$

$$\frac{\partial L}{\partial \dot{q}_f} = \rho \dot{q}_f \int_0^l \phi^2 \, dx - \rho \dot{q} \int_0^l x\phi \, dx \tag{C-29}$$

$$\frac{d}{dt}\left(\frac{\partial L}{\partial \dot{q}_f}\right) = \rho \ddot{q}_f \int_0^l \phi^2 \, dx - \rho \ddot{q} \int_0^l x\phi \, dx \tag{C-30}$$

$$-\frac{\partial L}{\partial q_f} = -\rho \dot{q}^2 q_f \int_0^t \phi^2 \, dx + EI q_f \int_0^t (\phi'')^2 \, dx + \rho g \int_0^l \phi \, dx \cos(q) \tag{C-31}$$

Then, after some rearranging, the Lagrange equations become

$$\underbrace{\begin{bmatrix} \frac{1}{3}\rho l^3 + \rho q_f^2 \int_0^l \phi^2 \, dx & -\rho \int_0^l x\phi \, dx \\ -\rho \int_0^l x\phi \, dx & \rho \int_0^l \phi^2 \, dx \end{bmatrix}}_{M} \begin{bmatrix} \ddot{q} \\ \ddot{q}_f \end{bmatrix} + \underbrace{\begin{bmatrix} \rho q_f \dot{q}_f \int_0^l \phi^2 \, dx & \rho \dot{q} q_f \int_0^l \phi^2 \, dx \\ -\rho \dot{q} q_f \int_0^l \phi^2 \, dx & 0 \end{bmatrix}}_{C} \begin{bmatrix} \dot{q} \\ \dot{q}_f \end{bmatrix}$$
$$+ \underbrace{\begin{bmatrix} 0 & 0 \\ 0 & EI \int_0^l (\phi'')^2 \, dx \end{bmatrix}}_{K} \begin{bmatrix} q \\ q_f \end{bmatrix} + \underbrace{\begin{bmatrix} -\frac{1}{2}\rho g l^2 & -\rho g \int_0^l \phi \, dx \\ \rho g \int_0^l \phi \, dx & 0 \end{bmatrix}}_{G} \begin{bmatrix} \cos(q) \\ q_f \sin(q) \end{bmatrix} = \begin{bmatrix} \tau \\ 0 \end{bmatrix} \tag{C-32}$$

Quick sanity check

It is useful to apply a sanity check. For an extension of 27m the mass per metre will be 283.70kg m^{-1}. The E-modulus of steel is 200GPa, using $I_{yy} = 0.0047m^4$, EI becomes $9.4 * 10^8 \text{N m}^2$. The modeshape used is normalized to $\int_0^l \phi_i(x)^2 \, dx = l$. The integrals used in the equations have the following numerical values:

$$\int_0^l \phi^2 \, dx = 27 \qquad \int_0^l x\phi \, dx = 414.6726 \tag{C-33}$$

$$\int_0^l (\phi'')^2 \, dx = 6.2782 * 10^{-4} \qquad \int_0^l \phi \, dx = 21.1407 \tag{C-34}$$

The beam is in horizontal position and in rest, equation C-32 becomes

$$\begin{bmatrix} 0 \\ EI \int_0^l (\phi'')^2 \, dx * q_f \end{bmatrix} + \begin{bmatrix} -\frac{1}{2}\rho g l^2 \\ \rho g \int_0^l \phi \, dx \end{bmatrix} = \begin{bmatrix} \tau \\ 0 \end{bmatrix} \tag{C-35}$$

This results in:

$$\tau = -10.142 * 10^5 \mathrm{N\,m} \tag{C-36}$$

$$q_f = -0.0997 \tag{C-37}$$

And a deflection of

$$w(l) = \phi(l) q_f = 2 * -0.0997 = -0.1994\mathrm{m} \tag{C-38}$$

This deflection corresponds with the deflection calculated with simple beam theories.

Bibliography

[1] M. Paskin, "Lewek falcon," 2016, [Accessed September 28, 2017]. [Online]. Available: https://www.flickr.com/thulobaba

[2] Windcat Workboats BV, "Windcat 10," 2008, [Accessed September 28, 2017]. [Online]. Available: http://www.windcatworkboats.com/

[3] J. Oelker, "Alpha Ventus & helicopter," 2015, [Areva Multibrid, accessed September 28, 2017]. [Online]. Available: https://www.offshore-stiftung.de/en/

[4] BHO, "BM-PR206-EN-DC-C-0124-Rev0 Time traces for BRR," Barge Master, Tech. Rep., 2015.

[5] Vroon Offshore Services, "VOS Start," 2017, [Ship image]. [Online]. Available: http://www.vroon.nl/fleet

[6] A. D. Luca, "Robots with Flexible Links: Modeling and Control," 2003, bertinoro (FC), 14-16 Luglio 2003.

[7] G. Hundleby and K. Freeman, "Unleashing europe's offshore wind potential: A new resource assessment," WindEurope, Tech. Rep., 2017.

[8] W. Pawlus, M. Choux, and M. R. Hansen, "Hydraulic vs. electric: A review of actuation systems in offshore drilling equipment," *Modeling, Identification and Control*, vol. 37, no. 1, pp. 1–17, 2016.

[9] J. van der Tempel, D. Cerda Salzmann, J. Koch, F. Gerner, and A. Göbel, "Vessel, motion platform, method for compensating motions of a vessel and use of a stewart platform," U.S. Patent 08 672 288, Mar. 18, 2014. [Online]. Available: https://patentscope.wipo.int/search/en/detail.jsf?docId=US43540702

[10] J. van der Tempel, D. Cerda, J. Koch, F. Gerner, and Göbel, "Ampelmann demonstrator: completion of a motion compensation platform for offshore access," in *Proceedings of European Offshore Wind Conference: Berlin, Germany*, 2008.

[11] Uptime, "Uptime 23,4m amc gangway accessing the trianel borkum west wind turbines and substation," YouTube, 2013. [Online]. Available: https://youtu.be/-Yzo4tLBClw

[12] Ampelmann, "O-type," accessed 11-10-2017. [Online]. Available: http://www.ampelmann.nl/systems/o-type

[13] Uptime, "Uptime undertun prototype 8m gangway for wind turbine access," YouTube, 2013. [Online]. Available: https://youtu.be/qo9sQ-laQ1s

[14] W. J. Pierson and L. Moskowitz, "A proposed spectral form for fully developed wind seas based on the similarity theory of sa kitaigorodskii," *Journal of geophysical research*, vol. 69, no. 24, pp. 5181–5190, 1964.

[15] D. Hasselmann, M. Dunckel, and J. Ewing, "Directional wave spectra observed during jonswap 1973," *Journal of physical oceanography*, vol. 10, no. 8, pp. 1264–1280, 1980.

[16] L. H. Holthuijsen, *Waves in oceanic and coastal waters*. Cambridge university press, 2010.

[17] BWA, "BM-PR206-EN-DC-M-0214-Rev0 Memo MRU drift," Barge Master, Tech. Rep., 2016.

[18] PTO, "BM-PR206-EN-ST-M-0248-Rev0 Interface forces gangway tip with offshore structure," Barge Master, Tech. Rep., 2017.

[19] E. R. Alphonsus and M. O. Abdullah, "A review on the applications of programmable logic controllers (plcs)," *Renewable and Sustainable Energy Reviews*, vol. 60, pp. 1185–1205, 2016.

[20] B. Walgaard, "Modeling and control of the motion compensated gangway, literature survey." Master's thesis, Delft University of Technology, 2017.

[21] T. Boaventura, M. Focchi, M. Frigerio, J. Buchli, C. Semini, G. A. Medrano-Cerda, and D. G. Caldwell, "On the role of load motion compensation in high-performance force control," in *Intelligent Robots and Systems (IROS), 2012 IEEE/RSJ International Conference on*. IEEE, 2012, pp. 4066–4071.

[22] H. Dallali, G. A. Medrano-Cerda, M. Focchi, T. Boaventura, M. Frigerio, C. Semini, J. Buchli, and D. G. Caldwell, "On the use of positive feedback for improved torque control," *Control Theory and Technology*, vol. 13, no. 3, pp. 266–285, 2015.

[23] H. Seraji and R. Colbaugh, "Force tracking in impedance control," *The International Journal of Robotics Research*, vol. 16, no. 1, pp. 97–117, 1997.

[24] F. Schiavo, L. Viganò, and G. Ferretti, "Object-oriented modelling of flexible beams," *Multibody System Dynamics*, 2006.

[25] R. J. Theodore and A. Ghosal, "Comparison of the assumed modes and finite element models for flexible multilink manipulators," *The International journal of robotics research*, vol. 14, no. 2, pp. 91–111, 1995.

[26] A. D. Luca, "Flexible Robots," *Encyclopedia of Systems and Control*, no. 1994, pp. 1–9, 2014.

[27] M. Saad, L. Saydy, and O. Akhrif, "Noncollocated passive transfer functions for a flexible link robot," in *Computer-Aided Control System Design, 2000. CACSD 2000. IEEE International Symposium on.* IEEE, 2000, pp. 30–34.

[28] D. Wang and M. Vidyasagar, "Transfer functions for a single flexible link," *The International journal of robotics research*, vol. 10, no. 5, pp. 540–549, 1991.

[29] F. Axisa and P. Trompette, "Modelling of Mechanical Systems," in *Modelling of Mechanical Systems: Structural elements.* Kogan Page Science, 2005, vol. 2, pp. 200–202.

[30] M. Saad, *Modeling of a One Flexible Link Manipulator.* INTECH Open Access Publisher, 2010.

[31] M. Saad, "Nonlinear control of a one flexible link in the vertical plane," in *Systems, Man and Cybernetics, 2007. ISIC. IEEE International Conference on.* IEEE, 2007, pp. 1579–1583.

Glossary

List of Acronyms

TU Delft	Delft University of Technology
MCG	Motion Compensated Gangway
PLC	Programmable Logic Controller
BRR	Bosch Rexroth
RAO	response amplitude operator
$\mathbf{H_{sig}}$	significant wave height
CFD	computational fluid dynamics
MRU	Motion Reference Unit
IMU	Inertial Measurement Unit
PSD	power spectral density
GPS	global positioning system
HPU	hydraulic power unit
HNC	Hydraulics-capable NC Control